

Full-Body Torque-Level Non-linear Model Predictive Control for Aerial Manipulation

Josep Martí-Saumell Joan Solà Angel Santamaria-Navarro Juan Andrade-Cetto

Abstract—Non-linear model predictive control (nMPC) is a powerful approach to control complex robots (such as humanoids, quadrupeds or unmanned aerial manipulators (UAMs)) as it brings important advantages over other existing techniques. The full-body dynamics, along with the prediction capability of the optimal control problem (OCP) solved at the core of the controller, allows to actuate the robot in line with its dynamics. This fact enhances the robot capabilities and allows, *e.g.*, to perform intricate maneuvers at high dynamics while optimizing the amount of energy used. Despite the many similarities between humanoids or quadrupeds and UAMs, full-body torque-level nMPC has rarely been applied to UAMs.

This paper provides a thorough description of how to use such techniques in the field of aerial manipulation. We give a detailed explanation of the different parts involved in the OCP, from the UAM dynamical model to the residuals in the cost function. We develop and compare three different nMPC controllers: Weighted MPC, Rail MPC and Carrot MPC, which differ on the structure of their OCPs and on how these are updated at every time step. To validate the proposed framework, we present a wide variety of simulated case studies. First, we evaluate the trajectory generation problem, *i.e.*, optimal control problems solved offline, involving different kinds of motions (*e.g.*, aggressive maneuvers or contact locomotion) for different types UAMs. Then, we assess the performance of the three nMPC controllers, *i.e.*, closed-loop controllers solved online, through a variety of realistic simulations. For the benefit of the community, we have made available the source code related to this work.

Index Terms—unmanned aerial manipulation, optimal control, non-linear model predictive control, differential dynamic programming, locomotion

I. INTRODUCTION

An unmanned aerial manipulator (UAM) is in many ways very similar to a humanoid. Both robots have arms attached to bodies that can move around. They can push, grasp, manipulate, catch, move, turn, throw, pull and transport objects; they may lean, rest, jump, or draw on surfaces; or wave, signal or point at things or people. They always have to fight against gravity, as their platforms are naturally unstable and constantly tend to lose balance and fall. They want to be compliant with unexpected or inaccurately planned contacts, so as to keep the robot integrity. They are redundant, meaning

J. Martí-Saumell, J. Solà and J. Andrade-Cetto are with the Institut de Robòtica i Informàtica Industrial, CSIC-UPC, Llorens Artigas 4-6, Barcelona 08028 (e-mail: {jmarti, jsola, cetto}@iri.upc.edu).

A. Santamaria-Navarro is with the NASA-Jet Propulsion Laboratory, California Institute of Technology, Pasadena, CA 91109 USA (e-mail: angel.santamaria.navarro@jpl.nasa.gov).

This work was partially supported by the EU H2020 project GAUSS (H2020-Galileo-2017-1-776293), project EB-SLAM (DPI2017-89564-P), by the Spanish State Research Agency through the María de Maeztu Seal of Excellence to IRI (MDM-2016-0656). Part of this research was carried out at the Jet Propulsion Laboratory, California Institute of Technology, under a contract with the National Aeronautics and Space Administration. U.S. Government sponsorship acknowledged.

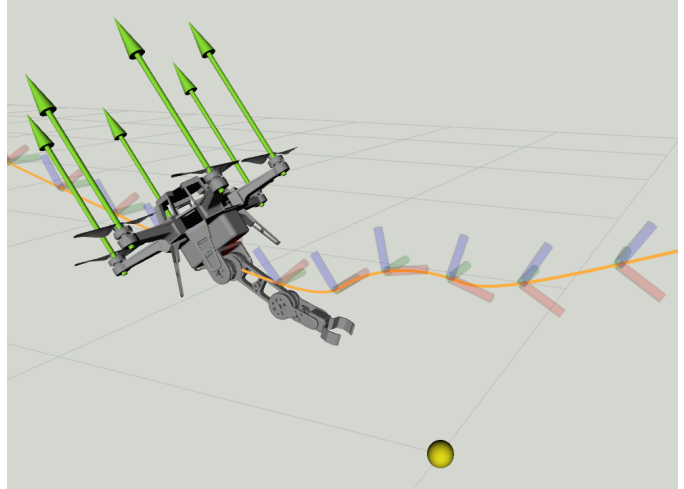


Fig. 1: Hexacopter with a 3DoF arm about to catch the ball in a non-stop flight maneuver, the *Eagle's Catch* maneuver, driven by a full-body, torque-level, non-linear model predictive controller. See the video of the paper at: <https://youtu.be/I-32ni4S2wg>.

that they can accomplish their tasks in different manners. They are underactuated, implying that they often have to plan complicated trajectories, with tricky dynamic maneuvers, to reach their goals (Fig. 1).

For all these reasons, these robots are similarly difficult to control, and the kinds of challenges they present are almost parallel. Yet the control approaches observed in the respective literature bodies are significantly different. One could think this is precisely because of the differences between them: flying versus walking. But we believe that these differences do not justify the diverging approaches. After all, we could add propellers to a humanoid, or make a multi-arm UAM walk or jump. At least at the conceptual level, what would then be the differences between these platforms? They would clearly vanish, suggesting a convergence of the control methods.

There are several aspects of motion control that are relevant to UAMs. Among others, we can highlight the following dichotomies, where the second options seem fairly desirable: separate base and arm controls vs. full-body control; kinematics vs. dynamics (*i.e.*, position or velocity control vs. torque control); and non-predictive vs. predictive control. The humanoids and the legged robots communities have undergone all these steps and converged to strategies of full-body optimal predictive control at the torque level. These formulations are at the same time generic, intuitive and powerful, have demonstrated their fitness to board many of the control challenges for such complex robots [1], especially when high dynamics are involved. In contrast, we have not seen these methods used in UAMs.

In view of this, in this paper we walk through the pro-

cess of adapting the full-body, torque-level, optimal control methods [1], [2], used in the communities of humanoids and legged robots to the field of UAMs. The use of full-body non-linear model predictive control (nMPC) simplifies the control architecture since it unifies several functional blocks. There are other advantages associated with using full-body nMPC. First, its genericity enables its usage by a wide variety of UAMs (*i.e.*, diverse multicopter platforms and manipulators) in a wide variety of tasks. The numerical approach to the problem allows to change the UAM with a small overhead on the modeling side, which is mostly automated. The control objectives as well as the constraints imposed by the system or the problem can be specified intuitively through cost functions and constraints in the optimal control problem (OCP) residing at the core of the nMPC. Besides, the prediction capability of this OCP allows to create and execute fast and aggressive motions that are in line with the dynamics of the robot. These dynamics can be properly exploited thanks to the force/torque control, thereby enabling the execution of tasks that would not be feasible statically. Finally, hybrid problems like walking or the pick-and-place operation (involving the change of the dynamic parameters) are easily modeled and handled with the optimal control approach.

Today, the OCP required in the nMPC techniques can be solved online. This is thanks to recent advances in fast non-linear solvers and efficient methods to numerically evaluate the dynamics of complex mechanical systems (such as legged robots, humanoids and UAMs). Of course, adapting the stated methods and implementing the related software does not suffice to enhance the capabilities of the current UAMs. In particular, progress on the hardware side is also required, *i.e.*, we need torque-controlled, rigid, and lightweight arms to mount on the flying platforms. Though we do not cover these aspects in the present paper, we do show through realistic simulations that the required electro-mechanic specifications can be achieved with currently available inexpensive hardware (especially motors, power electronics and low-weight CPUs) and mechanics (composite or 3D-printed arms).

A. Contribution & Paper outline

The contributions of this work include:

- 1) A thorough description to the approach, including the theory behind fast OCP solvers, the specification of the cost functions and the modeling of the dynamics.
- 2) Carrot-nMPC, a new strategy to specify the OCP in the nMPC that fully respects the optimality criteria used to define the mission. This is compared against previous approaches adapted from other fields of robotics.
- 3) A thorough validation through realistic simulation over a variety of platforms, arms and tasks, eventually involving high dynamics, providing evidence of computing times and hardware requirements that should allow real implementations in the immediate future.
- 4) All the software tools used to conduct the presented experiments in Section VII are made available for the benefit of the community.

The rest of the paper is structured as follows. In Section II, we give an overview of the state-of-the-art techniques related

to the control of UAMs. In Section III, we present the principal methods to solve OCPs, giving special attention to the fast solvers used in this work. The following two sections are devoted to explaining the formulation of the several parts involved in the OCP. In Section IV we explain how we build the dynamical model of the UAM, including the case where it is in contact with the environment. Then in Section V we show how we build the cost function by describing its structure as well as its different residual functions. In Section VI we present different strategies to move from the OCP used to generate trajectories offline, to online OCPs used to control the robots (nMPC). The described methods are finally tested in different experiments in Section VII. First, we present a set of UAM missions involving complex situations. These are solved offline to generate optimal state and control trajectories. Second, we compare the performance of different nMPC techniques for several platforms and tasks in a realistic real-time simulated environment. The paper closes in Section VIII with our conclusions.

II. STATE OF THE ART

A. Motion control

Motion controllers for UAMs can be divided into two categories [3], [4]. On the one hand, *decentralized controllers* control separately the platform and the robotic arm [5]. Hence, the respective controllers treat the interaction force as a disturbance. These methods are suited when the dynamics of the arm are insignificant, which makes the interaction force to be small. This can be achieved either by considering lightweight arms or by executing slow movements (*e.g.*, assuming zero roll and pitch angles of the base platform). A typical scheme for a decentralized approach is to consider a motion planner at the kinematic level, which normally resolves the kinematic redundancy of the UAM [6], [7] (*e.g.*, employing a hierarchical closed-loop inverse kinematic algorithm). Since it is common to have UAMs with arms controlled by position, these algorithms output conservative position set-points for the lower controllers of the platform and the arm, not only to minimize the interaction force but also to ensure that each controller reaches the desired positions within the required time.

On the other hand, *centralized controllers* do full-body control of the UAM. These are well-suited when the dynamics of the arm are significant. Among them, it is a common choice to apply feedback linearization. With fully-actuated platforms (like the one presented in [8]), we can design a control law that fully linearizes the dynamics of the system [9]. With under-actuated platforms, we can still linearize a portion of the dynamics by carefully choosing the output variable [10]. In any case, with the linearized (canceled) dynamics, the problem reduces to designing proper reference trajectories for the selected outputs. By assigning the proper dynamics to these outputs, one can create the output trajectories needed by the linearizing controller to drive the outputs to the desired value.

Alternatively, for *differentially flat*¹ systems, one could generate a sufficiently smooth trajectory in the *flat output*

¹Differential flatness is a property of a system that allows us to express the states and inputs as a function of several outputs and their higher order derivatives. These are the so-called *flat outputs*

space. This ensures that the system is able to follow the planned trajectory. Differential flatness implies feedback linearizability, which eases the application of a linearizing controller (see [11], [12] for further details on this equivalence). Proving that several outputs constitute a set of flat outputs involves manipulating the equations of the dynamics of the system. In aerial robotics, differential flatness was initially used for simple multicopter-based systems [13], [14]. When the complexity of the system increases, which is the case of UAMs, finding differentially flat outputs becomes a difficult task. In [15], [16] it is shown how a UAM can be differentially flat. However, this only holds if the first joint of the arm coincides with the center of mass of the platform. Moreover, the arm is restricted to be planar, *i.e.*, all the axes of the joints should be parallel, which severely limits its practical interest.

B. Environment interaction

Any UAM control technique should enable a fundamental capability: the interaction with the environment. In [17], they consider a fully-actuated hexacopter with a rigidly attached end-effector to solve several problems involving physical interaction. Ref. [18] proposes a UAM design with a 1-degree of freedom (DoF) arm to apply a force to a specific point. In [19], a fully-actuated platform with a 2-DoF arm is used to perform a “push & slide” maneuver in a cylindrical surface. The interaction considered in these approaches is limited to the application of forces on surfaces. However, the idea of leveraging the contact to create motion (*i.e.*, the contact-locomotion for UAM) has been rarely explored and, to the best of the authors’ knowledge, there exists only one reference exploring this path, [20], with a simplified 2D model of an UAM (*e.g.*, with a 1-DoF arm) hanging from a bar that is able to jump to another bar by exploiting the gripping contact.

Another common situation where UAMs interact with the environment involves load transportation pick and place operations. When catching or releasing the load, one should account for the changes in the dynamic parameters involved in these operations (addition of mass and change in the inertia matrix of one of the arm links).

C. Optimal control in aerial manipulation

There have been several works applying optimal control to aerial manipulation problems. Either solving the OCP online to control the robot using nMPC techniques, or offline as a trajectory generator. In [21], an nMPC controller at the kinematic level is used to generate set points for a low-level controller in a decentralized architecture. A closer approach to our current proposal can be found in [22], [23]. Even though they consider the full-body dynamics, both use OCP to generate a trajectory but not to control the UAM through nMPC. Besides, none of them consider contacts. In [24], a hybrid-nMPC is proposed to perform a writing task with a delta robot. That is, the OCP in the controller solves the problem at a force level for the platform and at the position level for the end-effector of the robotic arm. However, the dynamical model is simplified by considering quasi-static maneuvers.

To the best of the authors’ knowledge, full-body nMPC at the force/torque level has not been proposed for UAMs. However, there have been a few proposals involving single multicopters (not manipulators). In [25], a nMPC controller is used to track the attitude given by a higher level trajectory generator. An improved version is shown in [26], where the planning and the control blocks are unified. They use a sequential linear quadratic (SLQ) solver to solve, online, an OCP and apply the optimized thrust commands to the motors. A similar approach is taken in [27], where they consider the omnidirectional multicopter described in [28]. They use the derivative of the wrench on the body as the control variable in the nMPC, resorting to control allocation to retrieve the rotor speeds and tilt angles.

III. OPTIMAL CONTROL

An OCP is a specific type of optimization problem that mainly involves a dynamical system and a cost-function whose value depends on the evolution of this dynamical system. Its original continuous-time version has the following form:

$$\begin{aligned}
 \min_{\mathbf{x}(t), \mathbf{u}(t)} \quad & \int_{t=0}^T l(\mathbf{x}(t), \mathbf{u}(t)) dt + L(\mathbf{x}(T)) \\
 \text{s.t.} \quad & \dot{\mathbf{x}} = f_c(\mathbf{x}(t), \mathbf{u}(t)), t \in [0, T] && \text{(dynamics),} \\
 & \mathbf{x}_0 = \mathbf{x}(0) && \text{(initial value),} \\
 & h(\mathbf{x}(t), \mathbf{u}(t)) \geq 0 && \text{(path const.),} \\
 & r(\mathbf{x}(T)) \geq 0 && \text{(term. const.),}
 \end{aligned} \tag{1}$$

where $\mathbf{x}(t)$ and $\mathbf{u}(t)$ are respectively the state and control trajectories. The cost function is composed of the running cost given by $l(\mathbf{x}(t), \mathbf{u}(t))$ and the terminal cost, given by $L(\mathbf{x}(T))$. The dynamics constraint is represented by an ordinary differential equation (ODE) containing the model of the system (see Section IV for details on modeling a UAM). Besides, there is also the initial value constraint and, optionally, equality and inequality constraints for the state and the control trajectories.

We find two main approaches for solving the problem (1), [2]. On the one hand, the so-called *indirect methods* are based on finding optimality conditions for the continuous time problem. Eventually, these conditions are resolved numerically. Thus, they are also known as *first optimize, then discretize* methods. We can classify the indirect methods depending on the nature of their solution. Global indirect approaches are based on the Hamilton-Jacobi-Bellman (HJB) equation, which is derived by applying the dynamic programming principle to the continuous-time OCP. The big advantage of such methods is that they are able to give global optimal feedback policies. However, they are hardly applicable to complex systems due to the curse of dimensionality. This drawback is avoided in local indirect approaches, which apply the Pontryagin’s Minimum Principle (PMP), yielding necessary conditions for optimality. These conditions contain ODEs forming a two point boundary value problem (TPBVP) that can be solved numerically, *e.g.* using shooting or collocation methods. It is important to remark that, when solved, the obtained trajectories will only be candidate solutions since

PMP only offers necessary conditions for optimality, also known as *First Order Necessary Conditions*.

On the other hand, *direct methods* (also known as *first discretize, then optimize*) transcribe the continuous time formulation (*i.e.*, infinite-variable problem) (1) into a discretized version (*i.e.*, finite-variable) that takes the form of a non-linear programming (NLP) problem. That is (notice that we omit the path and terminal constraints for the sake of brevity),

$$\begin{aligned} \min_{\mathbf{X}, \mathbf{U}} \quad & \sum_{k=0}^{N-1} l_k(\mathbf{x}_k, \mathbf{u}_k) + L(\mathbf{x}_N) \\ \text{s.t.} \quad & \mathbf{x}_{k+1} = f(\mathbf{x}_k, \mathbf{u}_k), \quad k \in [0, N-1], \\ & \mathbf{x}_0 = \mathbf{x}(0), \end{aligned} \quad (2)$$

where $\mathbf{X} = \{\mathbf{x}_0, \dots, \mathbf{x}_N\}$ and $\mathbf{U} = \{\mathbf{u}_0, \dots, \mathbf{u}_{N-1}\}$ indicate, respectively, the set of states and controls that constitute the discrete trajectory. The dynamic constraint now has become a constraint for the states \mathbf{x}_k , \mathbf{x}_{k+1} and the control \mathbf{u}_k . The current $f(\mathbf{x}_k, \mathbf{u}_k)$ differs from its continuous time version in the sense that it contains the numerical integration of the ODE (see Section IV-A).

The discretized problem in (2) can be solved by any usual method aimed at solving constrained NLP problems [29]. These methods have become popular thanks to their simple and intuitive formulation. Besides, they allow the user to focus on such formulation, while leaving the solution to off-the-shelf solvers, *e.g.* IPOPT [30] or KNITRO [31]. These solvers usually rely on methods that perform big matrix factorizations when computing the search direction, something that in general implies to invert the Karush-Kuhn-Tucker (KKT) matrix. This slows down the solving process and, therefore, limits their application either to problems where the solving time is not an issue (*i.e.*, offline trajectory optimization (TO)) or nMPC with simple systems that allow an online solution of (2).

A. Differential Dynamic Programming (DDP)

Differential Dynamic Programming (DDP) [32] is a low-complexity algorithm that reduces the computational cost of solving (2), enabling the online solution for complex systems such as an UAM. DDP takes advantage of the Markovian character of the OCP and its resulting inherent sparsity: instead of factorizing one single big matrix, it performs several factorizations of many small matrices. Though DDP was presented over five decades ago, the method has recently regained attention in the robotics community due to its low computational requirements and also thanks to its new formulations, mainly represented by iterative linear quadratic regulator (iLQR) [33] and SLQ [34]. Using Gauss-Newton approximations, these formulations improve the speed of the original DDP algorithm and are common choices when applying nMPC to complex robotics systems like humanoids or quadrupeds [35].

The DDP method addresses the discretized OCP (2). DDP starts with a non-optimal trajectory for the controls $\mathbf{U} \triangleq \mathbf{u}_{0:N-1}$ and states $\mathbf{X} \triangleq \mathbf{x}_{0:N}$ and iteratively computes small improvements. This strategy resembles the local indirect methods, which are based on improving an existing trajectory. However, instead of solving the TPBVP to find an improvement for

the trajectory, DDP (like global indirect methods) relies on the dynamic programming technique. This is why it is normally considered to be an indirect method².

Each iteration of the DDP algorithm contains two principal steps or *passes*, which run over all the nodes (discretization points) of the trajectory: the *backward pass* and the *forward pass*. In the following we give the main formulation involved in these passes.

1) *Backward pass*: This pass results in an optimal policy at every node. We start the derivation of the equations involved in the backward pass by expressing the cost associated to the tail of the trajectory (from any node i until the terminal node N), *i.e.*,

$$J_i(\mathbf{x}_i, \mathbf{U}_i) = \sum_{k=i}^{N-1} l_k(\mathbf{x}_k, \mathbf{u}_k) + l_N(\mathbf{x}_N). \quad (3)$$

Thanks to the Bellman principle, we can recursively solve this problem as

$$\begin{aligned} V_i(\mathbf{x}_i) &\triangleq \min_{\mathbf{U}_i} J_i(\mathbf{x}_i, \mathbf{U}_i) \\ &= \min_{\mathbf{u}_i} [l_i(\mathbf{x}_i, \mathbf{u}_i) + V_{i+1}(f(\mathbf{x}_i, \mathbf{u}_i))], \end{aligned} \quad (4)$$

with $V_i(\mathbf{x}_i) \in \mathbb{R}$ being the *optimal cost-to-go* or *value* function. Then, DDP finds the local optimum of the following expression

$$\begin{aligned} Q_i(\delta \mathbf{x}_i, \delta \mathbf{u}_i) &= l_i(\mathbf{x}_i + \delta \mathbf{x}_i, \mathbf{u}_i + \delta \mathbf{u}_i) \\ &\quad + V_{i+1}(f(\mathbf{x}_i + \delta \mathbf{x}_i, \mathbf{u}_i + \delta \mathbf{u}_i)). \end{aligned} \quad (5)$$

For the sake of clarity, in the following the sub-indices i are omitted and the optimal *cost-to-go* at the next time step is shown with the prime symbol, *i.e.*, $V'(f(\mathbf{x}, \mathbf{u})) \triangleq V_{i+1}(f(\mathbf{x}_i, \mathbf{u}_i))$. The optimum of (5) is found by writing the quadratic approximation,

$$Q(\delta \mathbf{x}, \delta \mathbf{u}) \approx \frac{1}{2} \begin{bmatrix} 1 \\ \delta \mathbf{x} \\ \delta \mathbf{u} \end{bmatrix}^\top \begin{bmatrix} 0 & \mathbf{Q}_x^\top & \mathbf{Q}_u^\top \\ \mathbf{Q}_x & \mathbf{Q}_{xx} & \mathbf{Q}_{xu} \\ \mathbf{Q}_u & \mathbf{Q}_{xu}^\top & \mathbf{Q}_{uu} \end{bmatrix} \begin{bmatrix} 1 \\ \delta \mathbf{x} \\ \delta \mathbf{u} \end{bmatrix}, \quad (6)$$

and then optimizing with respect to $\delta \mathbf{u}$. The partial first- and second-order derivatives of (5) appearing in (6) are,

$$\mathbf{Q}_x = \mathbf{l}_x + f_x^\top \mathbf{V}'_x, \quad (7a)$$

$$\mathbf{Q}_u = \mathbf{l}_u + f_u^\top \mathbf{V}'_x, \quad (7b)$$

$$\mathbf{Q}_{xx} = \mathbf{l}_{xx} + f_x^\top \mathbf{V}'_{xx} f_x + \mathbf{V}'_x \cdot f_{xx}, \quad (7c)$$

$$\mathbf{Q}_{ux} = \mathbf{l}_{ux} + f_u^\top \mathbf{V}'_{xx} f_x + \mathbf{V}'_x \cdot f_{ux}, \quad (7d)$$

$$\mathbf{Q}_{uu} = \mathbf{l}_{uu} + f_u^\top \mathbf{V}'_{xx} f_u + \mathbf{V}'_x \cdot f_{uu}, \quad (7e)$$

where \mathbf{V}'_x , $(\mathbf{l}_x, \mathbf{l}_u)$, (f_x, f_u) and \mathbf{V}'_{xx} , $(\mathbf{l}_{xx}, \mathbf{l}_{ux}, \mathbf{l}_{uu})$, (f_{xx}, f_{ux}, f_{uu}) describe the Jacobians and Hessians of the value, cost and dynamics functions, respectively³.

²To solve the OCP by means of the DDP algorithm, we need first to discretize the problem. Thus, there exists literature where it is considered to be a direct method, *e.g.* [36]. In fact, if we consider the DDP algorithm as a black-box, it is indeed an NLP solver for problems with a Markovian structure.

³Note that the last terms of (7c)-(7e), denoting the product of a vector by a tensor, are not considered in the iLQR approach.

The minimization of (6) with respect to $\delta \mathbf{u}$ leads to the optimal policy

$$\delta \mathbf{u}^*(\delta \mathbf{x}) = \mathbf{k} + \mathbf{K} \delta \mathbf{x}, \quad (8)$$

with $\mathbf{k} \triangleq -\mathbf{Q}_{\mathbf{u}\mathbf{u}}^{-1} \mathbf{Q}_{\mathbf{u}}$ and $\mathbf{K} \triangleq -\mathbf{Q}_{\mathbf{u}\mathbf{u}}^{-1} \mathbf{Q}_{\mathbf{u}\mathbf{x}}$. If we insert this optimal policy into the quadratic expansion in (6), we obtain a quadratic approximation of the optimal *cost-to-go* as a function of $\delta \mathbf{x}$, *i.e.*

$$V(\delta \mathbf{x}) = \Delta V + \mathbf{V}_{\mathbf{x}}^{\top} \delta \mathbf{x} + \delta \mathbf{x}^{\top} \mathbf{V}_{\mathbf{x}\mathbf{x}} \delta \mathbf{x}, \quad (9)$$

where

$$\Delta V = -\frac{1}{2} \mathbf{k}^{\top} \mathbf{Q}_{\mathbf{u}\mathbf{u}} \mathbf{k}, \quad (10a)$$

$$\mathbf{V}_{\mathbf{x}} = \mathbf{Q}_{\mathbf{x}} - \mathbf{K}^{\top} \mathbf{Q}_{\mathbf{u}\mathbf{u}} \mathbf{k}, \quad (10b)$$

$$\mathbf{V}_{\mathbf{x}\mathbf{x}} = \mathbf{Q}_{\mathbf{x}\mathbf{x}} - \mathbf{K}^{\top} \mathbf{Q}_{\mathbf{u}\mathbf{u}} \mathbf{K}. \quad (10c)$$

We start the backward pass by assigning $V_N(\mathbf{x}_N) = L(\mathbf{x}_N)$ and then using the set of equations (7) to (10) to update recursively the optimal policy at each node.

Notice finally that at the optimum we will have $\mathbf{Q}_{\mathbf{u}} = \mathbf{0}$ and thus the optimal policy (8) becomes

$$\delta \mathbf{u} = \mathbf{K} \delta \mathbf{x}. \quad (11)$$

This optimal policy can be used outside the DDP algorithm as a state feedback law to modify the control commands in case of observed variations of the state \mathbf{x} .

2) *Forward pass*: Given a current guess of the trajectories (\mathbf{X}, \mathbf{U}) and the optimal policies computed during the backward pass, the forward pass applies appropriate modifications to them, node by node and proceeding forward,

$$\hat{\mathbf{x}}_0 = \mathbf{x}_0, \quad (12a)$$

$$\hat{\mathbf{u}}_k = \mathbf{u}_0 + \alpha \mathbf{k}_k + \mathbf{K}_k (\hat{\mathbf{x}}_k - \mathbf{x}_k), \quad (12b)$$

$$\hat{\mathbf{x}}_{k+1} \triangleq f(\hat{\mathbf{x}}_k, \hat{\mathbf{u}}_k), \quad (12c)$$

where the $\hat{\mathbf{x}}$ and $\hat{\mathbf{u}}$ are respectively the updated values for the states and controls. The assignment in (12c) implies the integration of the dynamics to update the next state. This procedure is also known as the *non-linear rollout*. The parameter $\alpha \in (0, 1]$ indicates the length of the step taken by the current iteration. A value of $\alpha = 1$ results in the application of a full step.

3) *Improvements*: In its original form, DDP has poor globalization capabilities, *i.e.*, from an arbitrary initial guess it struggles to converge to a good optimum. Mainly, this is due to the fact that DDP does not allow for infeasible trajectories during the optimization process, *i.e.*, the constraints $\mathbf{x}_{k+1} = f(\mathbf{x}_k, \mathbf{u}_k)$ have to be always fulfilled, like in a single shooting approach (see [2]). There have been several works trying to emulate a multiple shooting algorithm with DDP like *e.g.* [37] or [38] where they present a solver called Feasibility-prone Differential Dynamic Programming (FDDP), whose numerical behavior resembles the classical multiple shooting approach. FDDP considerably improves the globalization capability and the convergence rate of the solver.

Another limitation of the original DDP is its inability to handle constraints other than the ones imposed by the system

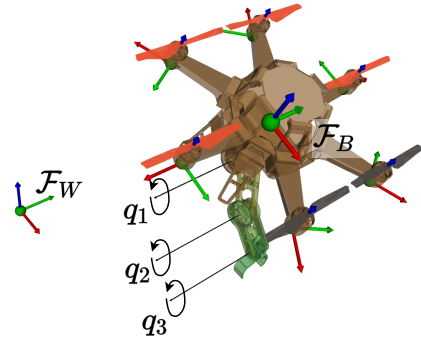


Fig. 2: Frame definitions for a typical UAM consisting of a planar hexacopter with a 3-DoF serial robot arm. \mathbf{q}_B represents the rigid transformation between \mathcal{F}_W and \mathcal{F}_B . In this case, $\mathbf{q}_J = [q_1, q_2, q_3]^{\top}$.

dynamics. This issue has been tackled differently in several works, *e.g.* [39], [40], [41].

In this paper, we use an improved version of the FDDP algorithm [38] that bounds the control inputs by means of a squashing function [42]. Other constraints are modeled as soft-constraints, that is, through quadratic barriers in the cost function.

IV. MODELING

A. Dynamics

The discrete-time evolution of the dynamical system from time t_k to time t_{k+1} has been defined in (2) as

$$\mathbf{x}_{k+1} = f(\mathbf{x}_k, \mathbf{u}_k). \quad (13)$$

This expression is used as a short-hand version of the true equation, defined with

$$\mathbf{x}_{k+1} = \mathbf{x}_k \oplus \int_{t_k}^{t_{k+1}} \dot{\mathbf{x}}(t) dt, \quad (14)$$

where the \oplus symbol stands for the right-plus operation on the manifold to which \mathbf{x} belongs [43], *i.e.*, $\mathbf{x} \oplus \mathbf{v} \triangleq \mathbf{x} \cdot \exp(\mathbf{v})$ for elements on non-linear manifolds such as the $SE(3)$ platform pose, and $\mathbf{u} \oplus \mathbf{v} \triangleq \mathbf{u} + \mathbf{v}$ for regular vectors such as velocities and joint angles. Evaluating (14) involves two main steps: *i*) the computation of the state derivative according to the continuous-time dynamical model of the platform, $\dot{\mathbf{x}}(t) = f_c(\mathbf{x}(t), \mathbf{u}(t))$; and *ii*) its numerical integration over the time step $\Delta t = t_{k+1} - t_k$. In this section we focus on specifying the model for the aerial manipulator (*i*), *i.e.*, on finding $\dot{\mathbf{x}}(t) = f_c(\mathbf{x}(t), \mathbf{u}(t))$. The integration is performed numerically, and the method used should ensure a good balance between accuracy and computational cost [44]. We use for this either the semi-implicit Euler or the Runge-Kutta RK4 methods, the latter being more costly but more accurate.

In the following, we express the pose of the flying platform or *base link* as an element $\mathbf{q}_B \in SE(3)$, and the configuration of the arm as a vector of the n_J joint angles $\mathbf{q}_J \in \mathbb{R}^{n_J}$ (Fig. 2). We note the robot's configuration as $\mathbf{q} = (\mathbf{q}_B, \mathbf{q}_J)$. Since we are interested in the dynamics, the robot state \mathbf{x} contains the configuration and its time derivative, $\mathbf{x} = \{\mathbf{q}, \dot{\mathbf{q}}\}$. The derivative of $SE(3)$ is a vector of linear and angular velocities in its tangent space $se(3)$, isomorphic to \mathbb{R}^6 , so that $\dot{\mathbf{q}}_B =$

$(\mathbf{v}, \boldsymbol{\omega}) \in \mathbb{R}^6$ and $\dot{\mathbf{q}} \in \mathbb{R}^{6+n_J}$. The state derivative $\dot{\mathbf{x}}$ can thus be represented by a regular vector $\dot{\mathbf{x}} = [\dot{\mathbf{q}}^\top, \ddot{\mathbf{q}}^\top]^\top \in \mathbb{R}^{12+2n_J}$.

The expression for $\dot{\mathbf{x}} = f_c(\mathbf{x}, \mathbf{u})$ can be written as,

$$\dot{\mathbf{x}} = \begin{bmatrix} \dot{\mathbf{q}} \\ \ddot{\mathbf{q}} \end{bmatrix} = \begin{bmatrix} \dot{\mathbf{q}} \\ FD(\mathbf{q}, \dot{\mathbf{q}}, \mathbf{u}) \end{bmatrix}, \quad (15)$$

of which we only need to find the accelerations $\ddot{\mathbf{q}}$. These result from the effect of all the forces applied to the robot, and can be found by computing the forward dynamics (FD). Here, we distinguish among two cases depending on whether or not the system's motion is constrained by external contacts. Both are detailed hereafter.

1) *Free flying phase*: When the robot is not subject to any contact constraining the motion, we can express the system equation of motion as [45]

$$\mathbf{H}(\mathbf{q})\ddot{\mathbf{q}} + \mathbf{C}(\mathbf{q}, \dot{\mathbf{q}}) = \boldsymbol{\tau}(\mathbf{u}), \quad (16)$$

where \mathbf{H} is the generalized inertia matrix, \mathbf{C} is a force vector containing the Coriolis, centrifugal and gravitational terms and $\boldsymbol{\tau}(\mathbf{u})$ is the joint generalized torque produced by the inputs \mathbf{u} (see Section IV-B). To compute the FD (*i.e.*, to isolate $\ddot{\mathbf{q}}$ from (16)) we do not necessarily need to compute \mathbf{H}^{-1} , which is expensive specially for complex robots. It is much more convenient to resort to the Articulated Body Algorithm (ABA), explained in [45], which significantly reduces the cost of computing the FD thanks to its recursive nature.

2) *Contact phase*: Any contact of a robot link with the environment constrains the robot's motion. In this paper, we account for rigid contacts, modeling them as implicit holonomic constraints, *i.e.*,

$$\phi(\mathbf{q}) = 0. \quad (17)$$

For example, a punctual contact of a link, with $\mathbf{p}_b(\mathbf{q})$ the point of contact belonging to the link, constrains the linear DoFs of the body at the environment's contact point \mathbf{p}_c , such as $\phi(\mathbf{q}) = \mathbf{p}_b(\mathbf{q}) - \mathbf{p}_c = 0$. As the contact in (17) is considered static, its time derivatives should also be null, *i.e.*,

$$\dot{\phi}(\mathbf{q}) = \mathbf{J}_c \dot{\mathbf{q}} = 0, \quad (18a)$$

$$\ddot{\phi}(\mathbf{q}) = \mathbf{J}_c \ddot{\mathbf{q}} + \dot{\mathbf{J}}_c \dot{\mathbf{q}} = 0, \quad (18b)$$

where $\mathbf{J}_c = \frac{\partial \phi}{\partial \mathbf{q}}$ is the contact Jacobian matrix, which maps the joint velocities to velocities at the contact point.

Thanks to the duality between velocity and force, this Jacobian's transpose \mathbf{J}_c^\top also maps each individual contact force to the joint-space [45]. These external forces, represented by $\boldsymbol{\lambda}$, affect the evolution of the system, so we add them to (16), yielding the new dynamics equation,

$$\mathbf{H}(\mathbf{q})\ddot{\mathbf{q}} + \mathbf{C}(\mathbf{q}, \dot{\mathbf{q}}) = \boldsymbol{\tau}(\mathbf{u}) + \mathbf{J}_c^\top \boldsymbol{\lambda}. \quad (19)$$

In order to solve this new FD problem we need to find the external forces $\boldsymbol{\lambda}$. This must be done subject to the constraint (17) and its time derivatives (18), which guarantee that the contact will remain static. Imposing that we reach the contact at zero velocity, that is without impact, we can ensure smooth trajectories for all variables (otherwise (19) would become singular at the contact instant). Then, we can find the joint acceleration and the contact forces by solving

the system formed by equations (19) and (18b), which can be posed in compact form as,

$$\begin{bmatrix} \mathbf{H} & \mathbf{J}_c^\top \\ \mathbf{J}_c & \mathbf{0} \end{bmatrix} \begin{bmatrix} \ddot{\mathbf{q}} \\ -\boldsymbol{\lambda} \end{bmatrix} = \begin{bmatrix} \boldsymbol{\tau} - \mathbf{C}(\mathbf{q}, \dot{\mathbf{q}}) \\ -\dot{\mathbf{J}}_c \dot{\mathbf{q}} \end{bmatrix}. \quad (20)$$

Unfortunately, this form is not suited for the ABA algorithm, and the solving methods often resort to factoring the KKT matrix through Cholesky decomposition—see [45].

An alternative FD computation, explicitly solving only for $\ddot{\mathbf{q}}$, consists in applying the Gauss principle of least constraint [45], [46]. According to this, the resulting joint acceleration will be the closest one to a free motion acceleration, *i.e.*, the eventual acceleration of the system in the absence of contacts. This can be posed as the quadratic programming (QP) problem

$$\begin{aligned} \min_{\ddot{\mathbf{q}}} & \quad \frac{1}{2} \|\ddot{\mathbf{q}} - \ddot{\mathbf{q}}_{\text{free}}\|_{\mathbf{H}(\mathbf{q})}^2 \\ \text{s.t.} & \quad \mathbf{J}_c(\mathbf{q})\ddot{\mathbf{q}} + \dot{\mathbf{J}}_c(\mathbf{q})\dot{\mathbf{q}} = 0. \end{aligned} \quad (21)$$

Interestingly, the KKT conditions of optimality for (21) are given by (20), and so the Lagrange multipliers for solving (21) are precisely the vector $\boldsymbol{\lambda}$, which is implicitly found alongside $\ddot{\mathbf{q}}$. This renders the problems (20) and (21) equivalent. In other words, while $\boldsymbol{\lambda}$ represents the dual variables (or Lagrange multipliers) from an optimization perspective, it represents the contact forces from the mechanical perspective.

B. Actuation model

We express the relation between control and generalized force by means of a linear mapping

$$\boldsymbol{\tau}(\mathbf{u}) = \mathbf{G}\mathbf{u}. \quad (22)$$

The mapping matrix \mathbf{G} has to be properly set according to the robot's geometry. For instance, in a fully-actuated robot all DoFs are actuated and so \mathbf{G} is full-rank. However, this is not the case for most UAM since they are built upon planar multicopter platforms. To obtain an expression for \mathbf{G} , let us express \mathbf{G} as a block-diagonal matrix containing \mathbf{G}_B and \mathbf{G}_{arm} , with the latter mapping the arm joints' torques. In this work, we consider the arms are fully-actuated, *i.e.*, $\mathbf{G}_{\text{arm}} = \mathbf{I}_{n_J}$. On the other hand, the matrix \mathbf{G}_B maps controls to the generalized force applied to the flying platform. Hence, \mathbf{G}_B synthesizes information about the geometry of the flying platform, *i.e.*, the number of propellers, how they are distributed and how their axes of rotation are placed. All these factors will make a significant impact on the behavior of the UAM. For example, the platform can be under-actuated if all the axes of the propellers are perpendicular to the platform. Contrarily, they can be strategically tilted so that the platform becomes fully-actuated. The remaining of this section is devoted to properly define \mathbf{G}_B .

Let us consider a reference frame $\{\mathcal{B}\mathbf{p}_i, \mathbf{R}_{B,i}\}$ for each propeller i , expressed in the base link reference, whose z axis is aligned with the propeller's rotation axis (see Fig. 2). Let u_i be the thrust generated by the i -th propeller and used as control input to the system (the thrust of a propeller is well approximated by the square of its rotational velocity, $u_i =$

$c_f \omega_i^2$). This thrust produces an external force to the multirotor platform, which has the expression

$${}^B \mathbf{f}_{i,th} = u_i \mathbf{R}_{B,i} \mathbf{e}_3, \quad (23)$$

where \mathbf{e}_3 is the standard unit vector along the z direction. For the same rotor i , the resulting couple ${}^B \mathbf{n}_{B,i}$ applied to the platform comes from the displaced thrust and from the drag moment, that is,

$${}^B \mathbf{n}_{B,i} = {}^B \mathbf{p}_i \times \mathbf{f}_{i,th} + (-1)^{CCW} u_i \frac{c_m}{c_f} \mathbf{R}_{B,i} \mathbf{e}_3, \quad (24)$$

where c_m and c_f are constants related to the propeller's geometry. If the spinning rotation of the i -th rotor is *counter-clockwise*, $(-1)^{CCW}$ evaluates to -1 , and to 1 otherwise. Stacking both the force and the couple for the i -th propeller, we get the i -th column for the matrix \mathbf{G}_B , *i.e.*,

$$\begin{aligned} \boldsymbol{\tau}_{B,i} &= \mathbf{g}_i u_i \\ &= \begin{bmatrix} \mathbf{R}_{B,i} \mathbf{e}_3 \\ {}^B \mathbf{p}_i \times \mathbf{R}_{B,i} \mathbf{e}_3 + (-1)^i \frac{c_m}{c_f} \mathbf{R}_{B,i} \mathbf{e}_3 \end{bmatrix} u_i. \end{aligned} \quad (25)$$

The matrix \mathbf{G}_B results from writing the above for all propellers in matrix form,

$$\boldsymbol{\tau}_B = \begin{bmatrix} \mathbf{g}_1 & \cdots & \mathbf{g}_{n_{prop}} \end{bmatrix} \begin{bmatrix} u_1 \\ \vdots \\ u_{n_{prop}} \end{bmatrix} \triangleq \mathbf{G}_B \mathbf{u}_{prop}. \quad (26)$$

V. COST FUNCTION

The two essential parts of an OCP are the system dynamic constraints, which approximate the behavior of the real UAM (see Section IV), and the cost function, which specifies the optimality criteria for fulfilling the tasks. The latter represents an intuitive manner to specify control objectives. A proper engineering of the cost function and a good weight tuning are crucial to obtain the desired trajectories that drive the UAM to fulfill required tasks. In this section we specify the main structure of a cost function along a trajectory and describe some typical residuals (costs) that are useful when applying optimal control to aerial manipulation.

A. Structure

We structure missions by a concatenation of movements or *phases*, which we divide in two main types: task phases and navigation phases (see Fig. 3). Task phases correspond to the periods of time where the robot is required to do something specific or to be somewhere. Waypoints, contacts or manipulations are considered tasks. They are typically implemented through quadratic costs on (parts of) the state, or on functions of the state. Navigation phases correspond to the periods of time when the robot flies freely from a finished task to the next. They are mainly constrained by the robot dynamics model. Navigation often requires the execution of maneuvers that exploit the full-body dynamics of the robot. This is

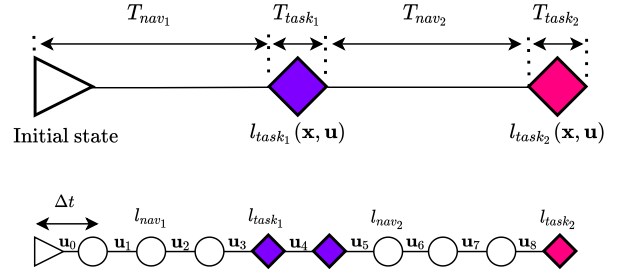


Fig. 3: Top: trajectory specification considering two tasks and two navigation phases. Bottom: a possible translation to an OCP, containing a series of nodes uniformly distributed in time.

especially true when dealing with under-actuated platforms.⁴ These maneuvers are discovered by the optimization process, provided that the time allocated to the navigation phase is sufficient.

In this work, the timing for each phase will be determined beforehand. For each phase we shall specify its duration T_{ph} and the structure of the residual (cost). Given this timeline, optimization will be performed with respect to states and control, discretized over a series of nodes with a uniform sampling time Δt (Fig. 3). Given a phase duration T_{ph} , the phase's number of nodes in the OCP is given by $N_{ph} = \frac{T_{ph}}{\Delta t} + 1$. Generally the costs are written as the squared weighted 2-norms of different residuals, yielding least-squares formulations which are easy to handle. Thus, the cost function for the k -th node related to a specific phase with R_{ph} associated residuals is

$$l_{k,ph}(\mathbf{x}_k, \mathbf{u}_k) = \sum_{i=1}^{R_{ph}} w_i \|\mathbf{r}_i(\mathbf{x}_k, \mathbf{u}_k)\|_{\mathbf{W}_i}^2, \quad (27)$$

where $\mathbf{r}_i(\mathbf{x}_k, \mathbf{u}_k)$ is a vector-valued residual that specifies the i -th task for the k -th node (see below for residuals specifications), \mathbf{W}_i is a square weighting matrix, usually diagonal, $\|\mathbf{v}\|_{\mathbf{W}}^2 \triangleq \mathbf{v}^T \mathbf{W}^{-1} \mathbf{v} \in \mathbb{R}$ is the Mahalanobis norm squared and w_i is a scalar to weight the overall task cost.

Navigation phases often contain costs devoted to minimize the energy of the system or the control inputs, *i.e.*, regularization terms for the state and the controls. Instead, the task phases consider costs related to the task, for instance the deviation between the desired and current poses of a link. For this reason, the weights w_i associated to navigation costs are typically (much) smaller than those of the task costs. This lets the optimizer freely find the best navigation path while strongly enforcing the fulfillment of the tasks.

B. Typical residuals

In the following, we present a set of residuals useful for OCP tasks involving UAMs. These will be used in the experiments shown in Section VII.

⁴A simple toy example is the swing up maneuver for an acrobat, which is a double pendulum only actuated at the elbow. In order to reach the unstable equilibrium state from the stable equilibrium point, we need to plan a complex trajectory that uses the arm dynamics to put both links upright.

1) *State error*: A common manner to specify a task is by setting a desired state \mathbf{x}^* for a specific node. Thus, we can define a state residual as

$$\mathbf{r}_{\text{state},k} = \mathbf{x}^* \ominus \mathbf{x}_k = \begin{bmatrix} \text{Log}(\mathbf{M}_{B,k}^{-1} \mathbf{M}_{B,k}^*) \\ \mathbf{q}_{J,k}^* - \mathbf{q}_{J,k} \\ \dot{\mathbf{q}}^* - \dot{\mathbf{q}}_k \end{bmatrix}. \quad (28)$$

The operator \ominus stands for the difference between states expressed as a vector of the space tangent to the states' manifold (see [43]): for elements in non-linear manifolds we have $\mathbf{Y} \ominus \mathbf{X} \triangleq \text{Log}(\mathbf{X}^{-1}\mathbf{Y})$, and in vector spaces simply $\mathbf{y} \ominus \mathbf{x} \triangleq \mathbf{y} - \mathbf{x}$. With this in mind, we can very well define residuals involving only a part of the state, *e.g.*,

$$\begin{aligned} \mathbf{r}_{\text{pos},k} &= \mathbf{p}^* - \mathbf{p}_k && \text{(position)} \\ \mathbf{r}_{\text{ori},k} &= \mathbf{R}^* \ominus \mathbf{R}_k && \text{(orientation)} \\ \mathbf{r}_{\text{linv},k} &= \mathbf{v}^* - \mathbf{v}_k && \text{(lin. vel.)} \\ \mathbf{r}_{\text{angv},k} &= \boldsymbol{\omega}^* - \boldsymbol{\omega}_k && \text{(ang. vel.)} . \end{aligned}$$

2) *Control*: Similarly to the state residual, we can define a control residual as

$$\mathbf{r}_{\text{control},k} = \mathbf{u}^* - \mathbf{u}_k. \quad (29)$$

Normally, this residual is used as a regularization cost, considering $\mathbf{u}^* = \mathbf{0}$ and giving it a low weight.

3) *Pose and velocity of frames*: It is a common practice in robotics to add a desired task in the operational space, *e.g.* a desired pose for the end-effector. It might also be useful to define desired poses for any arbitrary frame \mathcal{F} in the robot. Thus,

$$\mathbf{r}_{\text{pose},k} = \mathbf{M}_{\mathcal{F}}^* \ominus \mathbf{M}_{\mathcal{F},k} = \text{Log}(\mathbf{M}_{\mathcal{F},k}^{-1} \mathbf{M}_{\mathcal{F}}^*), \quad (30)$$

where $\mathbf{M}_{\mathcal{F}}^*, \mathbf{M}_{\mathcal{F},k} \in SE(3)$ are the desired pose and the pose of the frame \mathcal{F} at the node k , respectively. These frames and their velocities can be obtained from the state, following the method in [45], by properly concatenating several frame transformations. Therefore, we can also specify a desired linear and/or angular velocity for a frame \mathcal{F} at node k , *i.e.*,

$$\mathbf{r}_{\text{velocity},k} = \mathbf{v}_{\mathcal{F}}^* - \mathbf{v}_{\mathcal{F},k}. \quad (31)$$

As before, we can define residuals involving only parts (position, orientation, etc.) of the frame.

4) *Contact cone*: When defining the contact model in Section IV-A2 we assumed null velocity at the contact point. However, depending on the direction of the contact force and the surface characteristics, slippages may occur. To avoid them, we constrain the contact forces to be inside the Coulomb's dry friction cone defined by the friction coefficient μ between the contact point and the surface. For computation purposes, we approximate the friction cone by a square pyramid, *i.e.*, we impose the conditions

$$|f_{c,x}| \leq \mu f_{c,z}, \quad (32a)$$

$$|f_{c,y}| \leq \mu f_{c,z}, \quad (32b)$$

$$f_{c,z} > 0, \quad (32c)$$

where $\mathbf{f}_c = [f_{c,x}, f_{c,y}, f_{c,z}]^\top$ is the contact force represented by $\boldsymbol{\lambda}$ in (19) expressed in the reference frame of the contact surface. Notice that we can express (32) in matrix form,

$$\mathbf{A} \mathbf{f}_c = \begin{bmatrix} 1 & 0 & -\mu \\ -1 & 0 & -\mu \\ 0 & 1 & -\mu \\ 0 & -1 & -\mu \\ 0 & 0 & -1 \end{bmatrix} \mathbf{f}_c \leq \mathbf{0}, \quad (33)$$

where we use component-wise inequality. In this paper we are considering a DDP solver that cannot handle this kind of hard constraints. We therefore add them as soft constraints in the cost function by means of a quadratic barrier, *i.e.*, through a residual whose five components are assigned according to

$$r_{\text{contact},k}^i = \begin{cases} 0 & \text{if } \mathbf{a}^i \mathbf{f}_c \leq 0, \\ \mathbf{a}^i \mathbf{f}_c & \text{if } \mathbf{a}^i \mathbf{f}_c > 0, \end{cases} \text{ for } i = 1, \dots, 5, \quad (34)$$

where \mathbf{a}^i represents the i -th row of the matrix \mathbf{A} above.

VI. NON-LINEAR MODEL PREDICTIVE CONTROL

Non-linear model predictive control (nMPC), also referred to as receding horizon control, is a closed-loop control strategy for non-linear systems in which the applied input is determined online by solving an open-loop optimal control problem (OCP, Section III) over a fixed prediction horizon.

A. Architecture

We designed an nMPC pipeline where each time step is triggered by the arrival of robot states, which are provided by some state estimation module. At every time step, the OCP's initial state is set with the new robot state, the cost function is updated, the OCP is solved and finally the first command is applied. This section covers important considerations to achieve a good real-time flow of all these operations.

By construction, the complexity of the FDDP algorithm used to solve the OCP online is linear with the number of nodes, N , cubic with the number of control variables, and linear with the number of iterations, n . It is a common practice to fix the number of iterations to a small value $n \gtrsim 1$ to keep the overall execution time under control. While this might terminate the OCP before full convergence, the control to apply is the oldest in the OCP and has already undergone $N \times n$ iterations, which is enough. With n fixed, and since we cannot reduce the number of decision variables (it is robot-dependent), the computing time is determined by the number of nodes. Given a node period Δt , the length of the receding horizon of the nMPC is simply $T_H = (N - 1)\Delta t$. Having a controller with a decent prediction capability T_H is fundamental to fully exploit the possibilities of an under-actuated system, because these depend on the ability of the OCP to discover non-trivial maneuvers. T_H can be made longer by increasing Δt , which in turn allocates more computing time, thus allowing for a higher N . Unfortunately, increasing Δt augments the granularity of the control, and also compromises the validity of the integration methods (Section IV), rendering the results inaccurate and/or the system unstable. It is therefore

imperative to find a good balance between the number of nodes N , the prediction horizon T_H and the node period Δt .

The horizon T_H is typically shorter than the duration of the mission, T_M . This means that while most nodes of the OCP can be warm-started with the previous solution, the terminal (or horizon) node has to incorporate a new setpoint that is just beyond the previous horizon. These setpoints (*i.e.*, the residuals and the warm-start values) need to be determined based on mission information through some kind of mission plan. Since the granularity of the OCP is Δt , we need to bring the mission plan, which might be very sparsely specified, to something denser in time. An obvious strategy is to solve offline an OCP problem for the whole mission, and use it as a reference trajectory $\mathbf{X}^* = \{\mathbf{x}_0^*, \dots, \mathbf{x}_M^*\}$ to progressively feed the online OCP of the controller. For simplicity, it would be desirable to have the time step of the reference trajectory, Δt^* , equal to the OCP's Δt . However, we found that we require $\Delta t^* < \Delta t$ because the full mission OCP, which is much longer and usually not warm-started, is prone to instability and local minima when using large integration node periods. Due to this step difference, to feed this reference trajectory into the online OCP we have to interpolate the reference states \mathbf{x}_{k-}^* and \mathbf{x}_{k+}^* around the OCP's node k ,

$$\mathbf{x}_k = \mathbf{x}_{k-}^* \oplus s (\mathbf{x}_{k+}^* \ominus \mathbf{x}_{k-}^*), \quad (35)$$

where $s = (t_k - t_{k-})/\Delta t^* \in [0, 1]$ is the interpolation factor and \oplus, \ominus have been defined in Sections IV and V. Alternatively, we can also use FD to integrate the controls over \mathbf{x}_{k-}^* from t_{k-} to t_k , which is more accurate but also more expensive. Finally, notice that this larger OCP is slower to solve than the nMPC rate but, since we also use FDDP and we only have to solve it once, it is fast enough for a real-time operation. In case of a very large mission, we can break it into smaller overlapping sub-missions covering a few nMPC horizons each. We can then solve them online in a separate thread and have always references ready to feed the controller.

When the horizon reaches and then surpasses the end of mission at time T_M , we fill the OCP nodes beyond T_M with task nodes having the same terminal setpoint at T_M , that is $\mathbf{x}_{t \geq T_M} = \mathbf{x}_M^+$. This setpoint is required to be a statically stable state for the UAM – *e.g.* a hovering state or a landed state.

A common issue of nMPC controllers is the delay in the control command due to the computation time T_c of the solver. Given a state estimate $\hat{\mathbf{x}}(t_k)$ at time t_k , the optimal control to apply will only be known at $t_k + T_c$, and applying it at this late time would be suboptimal [47]. Having a predefined number of iterations allows us to anticipate this computation time. Thus, instead of solving the OCP with the first node at $\hat{\mathbf{x}}(t_k)$, we use a state $\hat{\mathbf{x}}(t_k + T_c)$ predicted using our dynamical model (14). After solving, we will have an optimal control to apply corresponding to the correct instant in time $t_k + T_c$ [36].

Finally, we cover the case where the refresh rate δt of the actuators' driver is (several times) faster than the node period, $\delta t < \Delta t$. In this case, we can compute optimal controls every δt using the optimal control policy (11) provided with the last solution of the FDDP solver. For this, we first need to predict a state $\mathbf{x}(t_u)$ at the control instant t_u using the dynamics model (14), then compute a state error $\delta \mathbf{x}$ with respect to

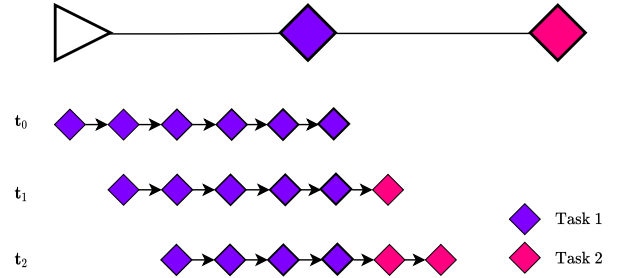


Fig. 4: Weighted MPC controller. Top: mission specification. Bottom rows: successive OCP of the W-MPC at three consecutive nMPC updates. Nodes have the same cost function as the closest task to come. Their increasing weights are set according to (36).

the estimated state at this same instant, $\delta \mathbf{x} = \hat{\mathbf{x}}(t_u) \ominus \mathbf{x}(t_u)$, and finally apply the control policy to find the controls.

After all these design considerations, we still have a lot of freedom to specify the OCPs at each time step. In the following, we present three nMPC strategies to build such OCP problems from the mission specification. The first two have been seen in the literature (although for tasks other than aerial manipulation), while the latter is a novelty of this paper.

B. Weighted MPC

This method is an adaptation from [48], which presents an nMPC controller to perform positioning tasks with a fully-actuated serial manipulator. The structure of the OCP in the weighted MPC (W-MPC) does not consider any node corresponding to a navigation phase. It also avoids computing the reference trajectory completely. Instead, each node adopts the cost function from the closest upcoming task (Fig. 4). The costs' weights $w_{i,k}$ take exponentially increasing values as nodes approach the task,

$$w_{i,k} = w_i e^{\alpha(t_k - t_{\text{task}})}, \quad (36)$$

where w_i is the task weight given in the mission specification, α is a tuning parameter that controls the sharpness of the increasing cost, $t_k = t_0 + k\Delta t$ is the time of the k -th OCP node, and t_{task} is the time when the next task starts. Notice that some other functions might be valid too, *e.g.* using a linear function or also assigning the weight according to a Gaussian envelope [26].

The main advantage of W-MPC is that it is simple. It has however important limitations that can be understood from the effects of the tuning parameter α , of the limited horizon, and of the absence of a proper warm start of the OCP (the reference trajectory). With α large, the only nodes with significant weight are the ones really close to the task. This makes the other nodes behave as navigation nodes, thus allowing the OCP to plan the optimal maneuvers to reach the task. However, if the task is beyond the horizon, this automatically drops all the weights to zero: the optimal solution becomes a null torque on all motors with the UAM falling to the ground. This is handled by setting the horizon node's weight to the task's weight w_i , with the effect of bringing the task to one horizon's time distance, thus hurrying the controls to achieve it, at occasions making it unfeasible because of the impossibility

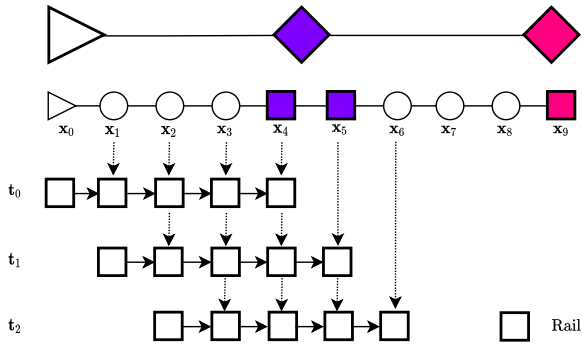


Fig. 5: Rail MPC controller. Top: mission specification. Mid: reference trajectory solved offline (circle: navigation node; square: task node). Bottom: successive OCP problems. At every nMPC update the desired state of each residual is updated with the corresponding state from the reference trajectory. All nodes become task nodes devoted to follow the reference closely, regardless of any disturbances.

to fit the appropriate maneuver. Notice that this strategy alters the optimality criterion set in the mission specification. Another option is to decrease α , thereby raising the weight of all the nodes within the horizon, now radically altering the mission’s optimality criterion. This has the adverse effect of eliminating the navigation nodes and therefore preventing non-trivial navigation maneuvers to emerge.⁵ Things get worse for under-actuated platforms because penalization costs on part of the state often prevent other parts to converge. For example, if the orientation during navigation is attracted to that of the task, then the platform tilts poorly and cannot accelerate to reach the destination. This must be alleviated by what we call here *underactuation-aware weighting (UAW)*, that is, weighting through \mathbf{W}_i in (27) the different parts of the state differently (*e.g.*, less weight on orientation than on position). UAW requires careful tuning, which renders W-MPC less simple than its original version. For all these reasons, this controller is only pertinent for fully-actuated platforms under low dynamics.

C. Rail MPC

The rail MPC (R-MPC) is basically a tracking controller (like the one presented in [27]). It tracks the reference trajectory $\mathbf{X}^* = \{\mathbf{x}_0^*, \mathbf{x}_1^*, \dots, \mathbf{x}_M^*\}$ that we get by solving a full-length OCP offline. This trajectory acts as the rail where the controller runs, hence the name of this controller. Notice that by solving this problem offline we already account for the high dynamics and the under-actuation of the system: the complex maneuvers will be discovered at the time of computing this reference trajectory.

The structure of the OCP considers the same type of residual for every node: tasks residuals attracting the trajectory towards the reference rail, and regularization residuals for the control (see Fig. 5), *i.e.*,

$$l_{rail,k}(\mathbf{x}_k, \mathbf{u}_k) = w_{state} \|\mathbf{r}_{state,k}\|_{\mathbf{W}_{state}}^2 + w_{ctrl} \|\mathbf{r}_{ctrl,k}\|_{\mathbf{W}_{ctrl}}^2. \quad (37)$$

⁵As a toy example, one can think of a pendulum with limited torque so that it has to perform a swing-up maneuver to drive the link to its upright equilibrium point. If the horizon is not long enough to accommodate the full swing-up maneuver, the controller will bring the link to a tilted position where the actuator torque equals the torque produced by the weight.

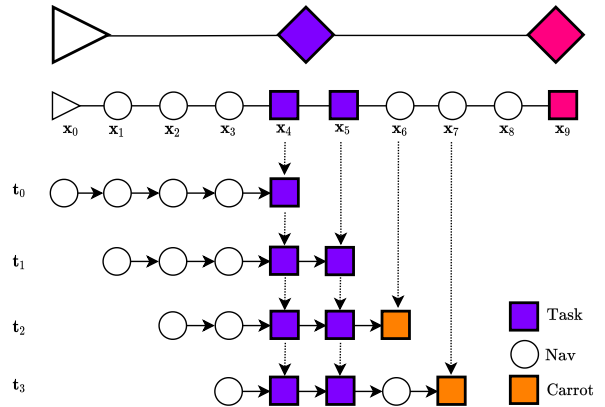


Fig. 6: Carrot MPC controller. Top: mission specification. Mid: reference trajectory solved offline (circle: navigation node; square: task node). Bottom: successive OCP problems. The carrot task node (orange square) is used to encode the optimal cost-to-go value function related to the original problem. Navigation nodes in the OCP provide the slackness needed to replan a new optimal trajectory in the event of a disturbance.

See Section V-B for more details on these residuals.

Using an nMPC controller as a tracking controller limits considerably its inherent re-planning capability, which is important in case of disturbances. The structure of its cost function restricts the solution to be the one that passes through \mathbf{X}^* . In the event of a disturbance, R-MPC outputs a set of controls to return to the nominal trajectory. These controls are no longer optimal due to the disturbance. Moreover, for under-actuated platforms and as it happened in W-MPC, we need to apply UAW to allow good convergence after disturbances towards the reference trajectory.

D. Carrot MPC

The carrot MPC (C-MPC) tackles the drawbacks of W-MPC and R-MPC. Departing also from a pre-computed reference trajectory \mathbf{X}^* we want a strategy able to control a UAM in highly dynamic maneuvers and with the ability to reject disturbances in an optimal manner, *i.e.*, by planning a new trajectory from the perturbed state, ignoring the reference trajectory. This reference is only used to set the horizon node of the OCP, which acts as the *carrot* that the UAM pursues.

The idea behind the C-MPC draws inspiration from the Bellman’s principle of optimality. This states that any optimal solution to a problem can be divided into several sub-problems whose solutions coincide with the original one. We apply it here by considering that beyond the horizon the optimal trajectory is given by the reference \mathbf{X}^* , while to reach the horizon we truly recompute a new optimal trajectory at each time (Fig. 6). The horizon node taken from the reference acts as the carrot. Through a task residual with sharp quadratic cost, this carrot node encodes the *cost-to-go* value function (4) from the horizon to the end of the mission. Notice that, unlike W-MPC and R-MPC, all except the task and carrot nodes are true navigation nodes. The part of trajectory with such nodes is *slack*, *i.e.*, arbitrary states or controls for these nodes have a small penalization in the cost function. This gives the controller the ability to recompute, online, a new

optimal trajectory towards the carrot or task states, whichever comes first, eventually discovering new maneuvers, with an optimality criterion that matches the one originally specified for the mission, and without any need for UAW or any other tuning.

VII. VALIDATION

The versatility of optimal control allows us to use it within a wide range of applications and situations involving UAMs (see Section I-A). We present in Section VII-A a number of examples involving different scenarios of trajectory optimization for full-body torque-controlled UAMs. See Table I for a summary of the trajectories. Then in Section VII-B we close the control loop to test the performance of the different nMPC controllers described in Section VI.

All OCPs in these experiments have been built with an open source C++ library delivered with this paper, called EAGLEMPC⁶. As a dependency to build and solve the OCP, we use CROCODDYL [38], which in turn uses PINOCCHIO [49] to compute the fast articulated body dynamics algorithms based on [45] such as the ABA. EAGLEMPC includes the implementation of the nMPC controllers explained in Section VI as well as the implementation of the SquashBox FDDP solver presented in [42]. Besides, we also provide specific tools to ease the assembly of optimization problems for UAMs, such as a YAML file parser to specify problems following the philosophy explained in Section V.

The simulations in Section VII-B use the GAZEBO⁷ simulator, and a modified version of ROTORS⁸ [50], which has been specialized to aerial manipulation. The Robot Operating System (ROS)⁹ packages needed to run nMPC controllers along with some other useful tools are also provided¹⁰. The rest of software dependencies along with further instructions on how to reproduce the experiments are collected in a specific repository¹¹. All these experiments have run single-threaded in a laptop with an Intel® Core™ i7-8750H CPU @ 2.20GHz × 12 with 32GB of RAM.

A. Trajectory optimization

In this section, we describe how we build OCPs for different missions with the costs considered for each phase. To showcase the abilities of the presented approach, we include challenging missions with the following characteristics (usually not considered in the state-of-the-art of aerial manipulation):

- **Aggressiveness:** trajectories with motions ranging from quasi-static (slow) to agile (fast) maneuvers.
- **Type of aerial manipulators:** we combine 3 different platforms, including a non-planar hexacopter [8], with 3 serial manipulators of different DoFs (see Table I).
- **Contacts:** we present some simulations with contacts between the aerial robot and the environment.

⁶<https://github.com/PepMS/eagle-mpc>

⁷<http://gazebosim.org/>

⁸https://github.com/PepMS/rotors_simulator

⁹<http://ros.org/>

¹⁰<https://github.com/PepMS/eagle-mpc-ros>

¹¹https://github.com/PepMS/fbtl_nmpc_experiments

TABLE I: Mission configurations and characteristics

	Eagle's catch	Monkey bar	Push & slide	Box deployment
PLATFORMS				
Hexacopter 370 (planar)	✓	✓		
Hexacopter 670 (planar)				✓
Tilthex (non-planar)			✓	
MANIPULATORS				
Serial link manipulator-2DoF				✓
Serial link manipulator-3DoF	✓	✓		
Serial link manipulator-5DoF			✓	
MISSION CHARACTERISTICS				
Aggressive	✓	✓		
Contacts	✓	✓	✓	
Model changes				✓

- **Model changes:** we provoke some sudden mass changes during the maneuvers.

To compute these trajectories we cold-start the solver, *i.e.*, the initial guess is a trajectory where all states and controls are zero. The platform and mission characteristics are detailed in Table I. Mission phases and costs are in Table II. The configuration of the OCP and its main performance indices come in Table III. The four missions are displayed in Fig. 7 — we strongly encourage the reader to look at the provided videos to appreciate the dynamics and full-body control. They are described and evaluated hereafter.

1) *Eagle's catch:* This mission emulates an eagle catching an animal on the ground. A detail of the catching maneuver is shown in Fig. 7a. The first part of the trajectory is meant to drive the end-effector to the catching point (phases 1 and 2). There, it transitions to the catching phase (phase 3), which contains a contact between the end-effector and the ground. This contact is modeled as a non-sliding 3D contact point to constrain the translation, allowing rotations around it. To ensure the validity of the contact modeling and avoid slippage, we have added a cost that penalizes forces out of the friction cone. Finally, the robot flies away towards a hovering point further on (phases 4 and 5).

The resulting control trajectory shows a remarkable maneuver discovered by the OCP during the catching phase (see Figs. 1, 7a and 8). Notice how the thrusts of the motors decay considerably, while the arm holds a small fraction of the UAM's weight in a quasi-singular configuration (arm straight, near-zero torques). The UAM is acting partially as a passive inverted pendulum, partially as in a ballistic parabolic path (observable in Fig. 1), consuming almost no energy. While this behavior might seem unnatural, it is however optimal given the specification. Two different approaches to a more realistic eagle's catch would be to impose a minimum flight velocity during the catch phase (a must in fixed-wing platforms), or to specify a contactless mission. We explore this last possibility in the nMPC experiments in Section VII-B.

2) *Monkey bar:* Inspired by [20], the aim of this experiment is to validate contacts as a useful source of motion for UAMs.

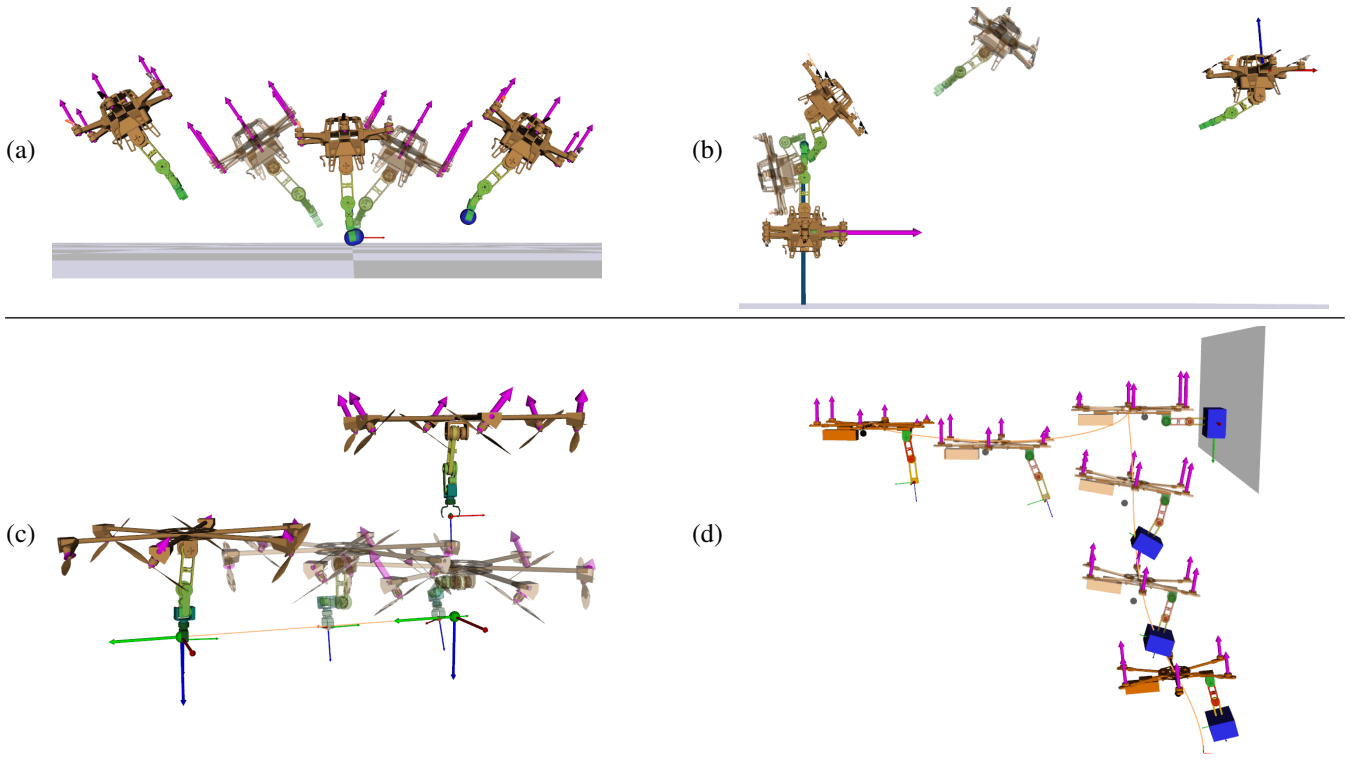


Fig. 7: Sequence of each mission. (a) *Eagle's Catch* with Hexacopter370 & 3DoF arm. (b) *Monkey-bar* with Hexacopter370 & 3DoF arm. (c) *Push & slide* with Tiltex & 5DoF arm. (d) *Box deployment* with Hexacopter680 & 2DoF arm. Click on images to see videos.

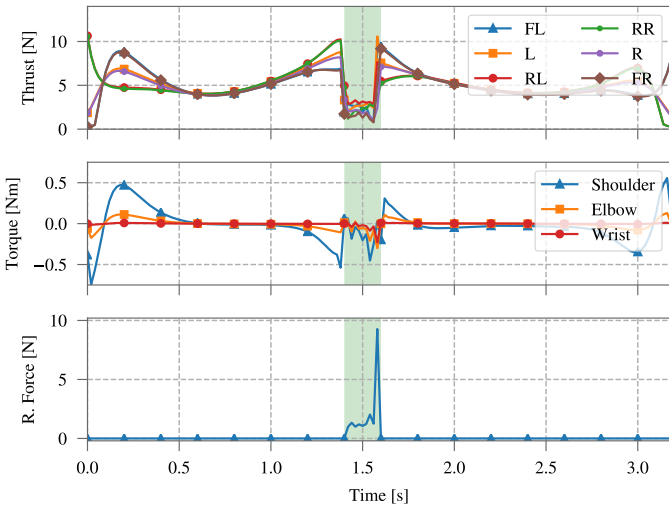


Fig. 8: *Eagle's Catch* mission. Top: platform motor thrust; Center: torque of the arm motors; Bottom: L_2 norm of the reaction force at the end-effector. Shaded area indicates the catching phase.

The experiment considers a UAM that is initially hanging upside down from a bar which it grasps with the end-effector. The objective is to bring the platform to a waypoint that is placed in front of the robot and above the ground (see Fig. 7b). We simulate an overloaded UAM by limiting the maximum thrust of its 6 propellers to 4N. This is insufficient to hold its total weight of 25N, and thus to be able to reach the waypoint the robot has to jump from the bar with its arm. The contact with the bar is modeled as a contact point that constrains the three linear DoFs.

The first phase includes the robot climb on top of the bar and the jump. Fig. 9 shows how, from 0s to approximately 0.75s, all motors are used to produce the climb to an upright position. From there, the robot gently leans forward to a final push to eventually jump from the bar (from 1s to approximately 1.4s). Notice how at the jump instant the arm is producing a maximum push against the bar of almost 200N. At this point the robot enters the flying phase, during which the actuators saturate at full throttle to hold the weight of the UAM. As the UAM approaches the waypoint they orient the platform so it can reach it with the desired pose. This pose corresponds to the only task in this trajectory (phase 3).

Interestingly, as the contact phase is significantly long, it may occur that the end-effector separates from the contact point due to a numerical drift when integrating the constraint $\phi(\mathbf{q}) = \mathbf{0}$. To ensure the numerical stability of the contact we have chosen a small integration step of $\Delta t = 5\text{ms}$ along with a Runge-Kutta (RK) integrator of 4-th order. This is a simple and sufficient approach here. One can use other techniques to improve the numerical stability for such constrained trajectories such as the addition of Baumgarte's gains [51].

3) *Tiltex push & slide*: This mission is meant to validate two key concepts. First, we want to show that the proposed formulation can deal with complex UAM designs. We use for this a UAM based on the fully-actuated *Tiltex* platform [8] with a non-planar 5DoFs manipulator (see Fig. 7c). The second idea is to check that an OCP approach can effectively solve interacting tasks that have been tackled so far with different approaches. For this, we choose a typical interaction problem, the so called *push & slide*, by which we push on a surface

TABLE II: OCPs' definitions. Costs specified for BL: base link; EE: end effector; L1: link 1. Phases N: navigation; T: task; C: contact.

	RESIDUAL TYPES						
	T_{phase} [s]	\mathbf{x}, \mathbf{u} reg. & \mathbf{x} bounds	Frame pose	Frame position	Frame orientation	Frame velocity	Friction cone: EE
EAGLE'S CATCH							
Phase 1: approach (N)	1.4	✓					
Phase 2: pre-catch (T, C)	-	✓		EE		EE	
Phase 3: catch (T, C)	0.1	✓		EE		EE	✓
Phase 4: fly away (N)	1.6	✓					
Phase 5: hover (T)	-	✓		BL		BL	
MONKEY BAR							
Phase 1: balancing (N, C)	1.4	✓		EE			
Phase 2: flying (N)	0.5	✓					
Phase 3: hover (T)	-	✓	BL				
PUSH & SLIDE							
Phase 1: approach (N)	1.5	✓					
Phase 2: pre P & S (T)	-	✓	EE	BL	BL	EE, BL	
Phase 3: P & S (T, C)	2.5	✓	EE	BL	BL	EE	
Phase 4: P & S end (T, C)	-	✓	EE	BL	BL	EE, BL	
BOX DEPLOYMENT							
Phase 1: approach (N)	2.0	✓					
Phase 2: anchoring (T)	1.0	✓	EE		L1	EE	
Phase 3: fly-away (N)	2.0	✓					
Phase 4: hover (T)	-	✓	BL			BL	

TABLE III: Solver performance

	Eagle's catch	Monkey bar	Push & slide	Box deployment
Duration T_M [s]	3.1	1.9	4	5
Node period Δt [ms]	20	5	20	20
# Nodes N	156	381	202	254
Integrator	SI-E ¹	RK4 ²	RK4	SI-E
# Iterations	22	181	80	29
Solving time [s]	0.21	11.9	4.4	0.25
per iteration [ms]	9.1	65.7	55.0	8.6
per node [μ s]	58	173	272	34
per # controls cubed [ns]	80	237	204	66

¹SI-E: Semi-implicit Euler

²RK4: 4-th order Runge-Kutta

with the end-effector while sliding it along a straight line path.

The mission starts by bringing the end-effector at the beginning of the push & slide path (phases 1 and 2). Phase 2 finishes when the robot is at disposal of starting the pushing phase. That is, the end-effector has a specific pose with a null velocity and the platform is parallel to the ground at specific height (see the costs of phase 2 in Table II). The height requirement for the platform is to make sure that the arm is away from singularities. The push & slide begins at phase 3 with the end-effector in contact with the surface (indicated by the green shaded area in Fig. 10). This contact is modeled

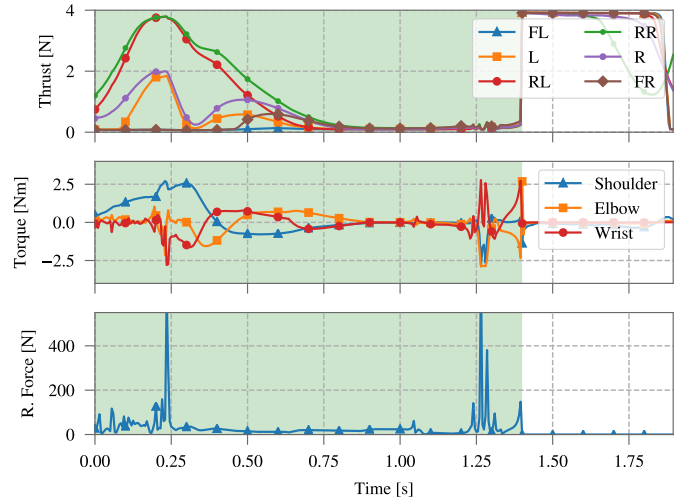


Fig. 9: Monkey bar mission. Top: platform motor thrust; Center: torque of the arm motors; Bottom: L_2 norm of the reaction force at the end-effector. Shaded area indicates the contact phase, which has two distinguished parts separated by a resting stage: climbing to the upright position, and jumping at $t = 1.4$ s.

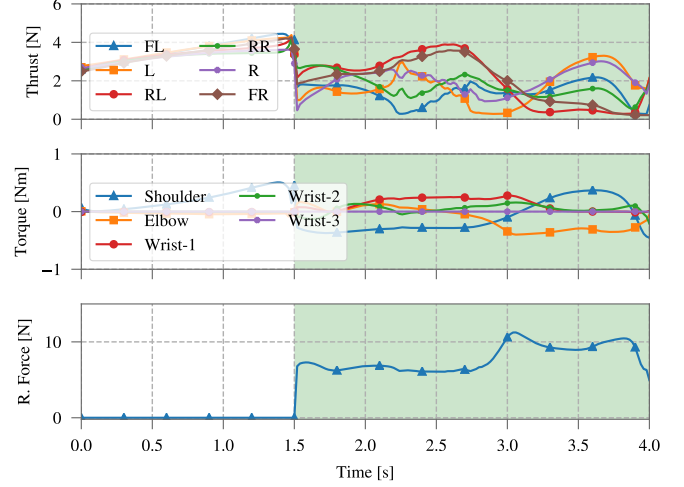


Fig. 10: Push & Slide mission. Top: platform motor thrust; Center: torque of the arm motors; Bottom: L_2 norm of the reaction force at the end-effector. Shaded area indicates the actual push & slide phase.

as a rolling contact along the forward (y) axis, constraining the linear movements in the lateral (x) and vertical (z) axes. To ease the convergence of the solver, we have added a cost penalizing the end-effector for deviating from the slide path.

4) *Box deployment*: This experiment validates the use of the OCP framework for situations where the model varies. We simulate the deployment of a 1kg self-anchoring package onto a wall (see Fig. 7d). Here, in order to ensure the proper placement of the box, we hold it at the same anchoring place for one second (mimicking a wall contact as in the case of a wall-grasping action). The deployment involves a switch between two different models, *i.e.*, with and without the box, implying important mass changes during the trajectory (*i.e.*, different parameters of the dynamic model).

We use a planar hexacopter with a planar 2DoF arm. A first navigation phase leads the end-effector and the box towards the anchoring pose. To avoid the collision between

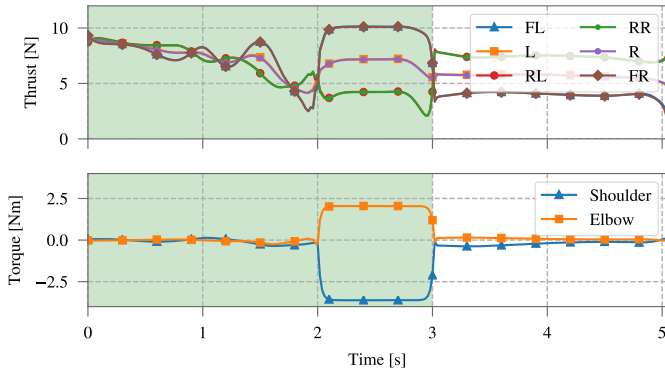


Fig. 11: Box deployment. Top: platform motor thrust; Bottom: torque of the arm motors. Shaded area indicates the phase carrying the load.

the propellers and the wall, we must ensure a fully extended configuration when the end-effector reaches the box deployment phase (phase 2). For this purpose, we have added a cost to enforce the orientation of link 1. During this phase, (from second two to second three) we can see in Fig. 11 how the front motors have to compensate for the displaced mass. The model switching occurs at the end of this phase 2 and the platform motors have to account for the sudden change of the center of mass of the robot (non-shaded area in Fig. 11).

B. Model Predictive Controllers

The aim of this section is to test the nMPC controllers presented in Section VI and verify experimentally the respective behaviors that we have anticipated.

In this section we do not deal with hybrid problems, which involve model switches due to contacts or changes of mass. Solving these problems within an nMPC framework requires additional reasoning and decisions that are out of the scope of this paper. For example, in the case of contacts we have to decide whether we feed the OCP with a predefined contact sequence or, differently, we endow the nMPC with the ability to decide the placements for the contacts ([35]). We could also allow for unplanned contacts to occur (with the result of impacts that would render the derivatives discontinuous) and implement a contact detector to, online, modify the dynamics model at the precise contact switching instants. These and other important algorithmic additions are not obvious and would deviate the focus of the present work. We believe that considering single-model problems suffices to validate the nMPC strategies that we have described.

All controllers share the same basic configuration. Their OCPs have $N = 30$ nodes separated $\Delta t = 30$ ms, which results in a horizon of $T_H = 870$ ms, and are limited to $n = 4$ iterations. Robot state estimates arrive every $\delta t = 2.5$ ms (i.e., 400Hz), triggering the OCP update and solving. We have tuned each controller to perform at its best. In particular, we use UAW in R-MPC and W-MPC, where the weights for the platform position and the arm joints' angles are set significantly higher than those of orientation and velocity.

1) *Underactuation*: We set two experiments, *4-Displacement* and *Eagle's Catch*, with different complexities

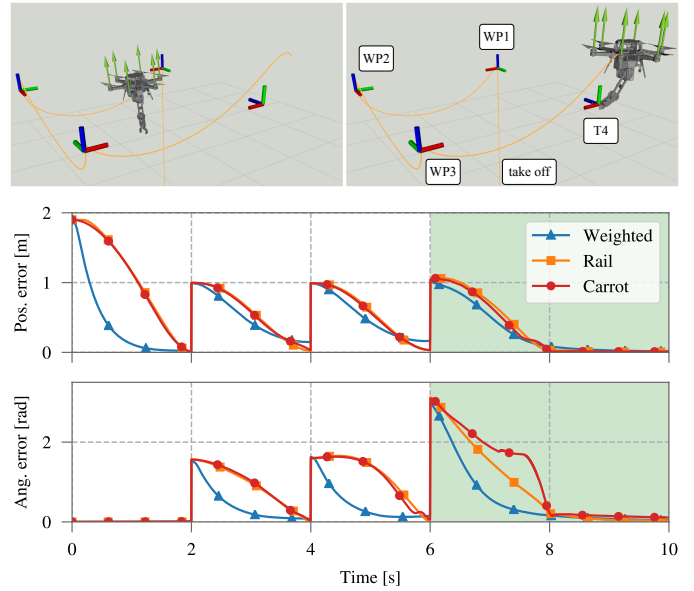


Fig. 12: The *4-Displacement* mission. Intermediate and final snapshots, and pose error of the incoming task for the three nMPC controllers. Pose waypoints $WP\{1,2,3\}$ for the platform at times $t = \{2, 4, 6\}$ s. Shaded area indicates a pose task T4 for the end effector at $t = 8$ s. Click on images to see video.

to test how each controller copes with the under-actuation of the platform, including slow and aggressive maneuvers.

The *4-Displacement* mission (Fig. 12) requires slow movements. It has four tasks to be accomplished at seconds 2, 4, 6 and 8, which are separated by navigation phases. The first three tasks $WP1-3$ specify a desired pose for the platform. The last task T4 specifies a desired pose for the end-effector and a desired hovering orientation for the platform. Fig. 12 shows the error norm of the pose residuals, with the three controllers managing to reduce the error for each task (notice that the error from 6s to 10s is related to the end-effector's desired pose). While R-MPC and C-MPC have similar levels of task accomplishments, the W-MPC shows larger position errors. This is because W-MPC adds the residuals of the task to every node in the horizon (see Fig. 4): the controls hurry to get to the task, which is good but far from optimal, but then struggle to truly converge due to insufficient UAW tuning. Since there are no significant disturbances, R-MPC and C-MPC execute the reference trajectory, which is optimal, with similar results. C-MPC can however react at the last moment to better reposition the end effector, a maneuver visible before second 8 in Fig. 12.

The performance differences between the three controllers are magnified when the trajectory becomes more aggressive. Hence, here we evaluate them with an *Eagle's Catch* mission where this time we are not considering the contact with the ground. Fig. 13 shows some snapshots around the catch task and the norm of the residuals from each controller. In this experiment, W-MPC fails to reach the grasping point due to its lack of prediction capability (see Section VI-B), while R-MPC and C-MPC behave satisfactorily.

2) *Disturbance rejection*: As seen in the previous experiments, with a proper UAW tuning of the weights in the R-

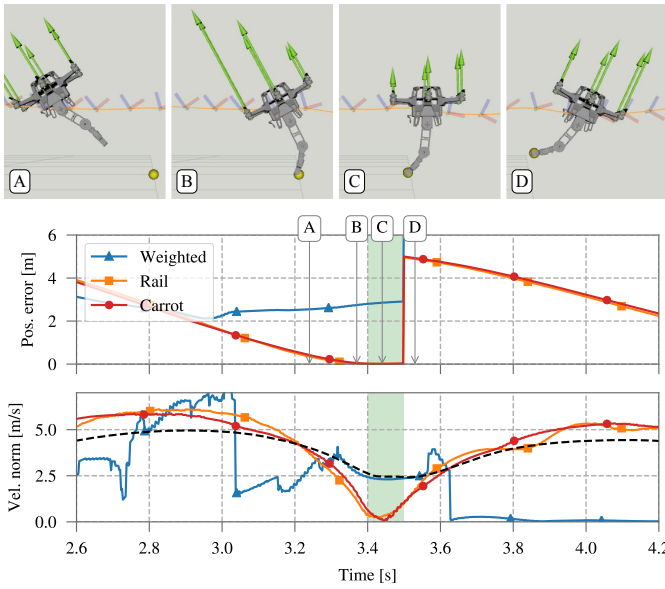


Fig. 13: The *Eagle's Catch* mission. Top: snapshots around the catch instant labeled A, B, C, D. Center: end effector position error during the approaching and catching phase. Bottom: Linear velocity norms of end effector (colors) and platform (dashed black, only C-MPC is shown). Shaded areas indicate the catching phase. Notice the anticipation and swing of the arm to be able to reach the object with the end effector at zero velocity while the platform flies at 2.5m/s. Notice also that C-MPC is smoother. Click on images to see video.

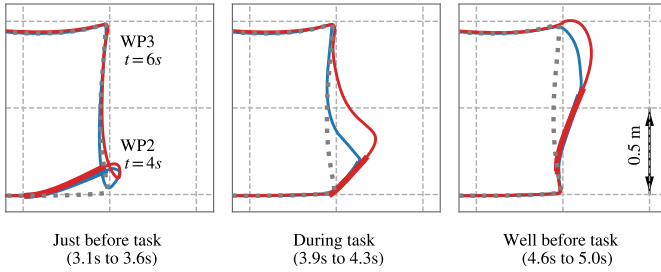


Fig. 14: XY trajectories for the *4-Displacement* experiment with disturbances starting at different times. Dotted gray: reference trajectory; Blue: R-MPC; Red: C-MPC. Thicker portion indicates the disturbance is active. While the R-MPC tries to return to the reference trajectory, the C-MPC re-plans a new optimal trajectory towards the next task. See Fig. 15 for the corresponding control signals. Click on images to see video.

MPC, both R-MPC and C-MPC can accomplish tasks with a similar precision to that of the offline computed trajectory. This is an expected behavior in nominal conditions with only small perturbations. However, differences between these two emerge when larger disturbances enter the scene. To evidence these, we have run three simulation case studies where three disturbances of 10N in the $[1, 1, 0]$ direction are applied to the robot during 0.4s while performing the *4-Displacement* mission. These disturbances come just before the task WP2, during the task WP2, and well before the next task WP3. The resulting platform trajectories are shown in Fig. 14. We see how R-MPC always tries to track the reference trajectory while C-MPC re-plans a new optimal trajectory to fulfill the tasks. This results in much more aggressive commands for the R-MPC (shown in Fig. 15), which work hard for regaining the reference trajectory even though this is not a requirement of

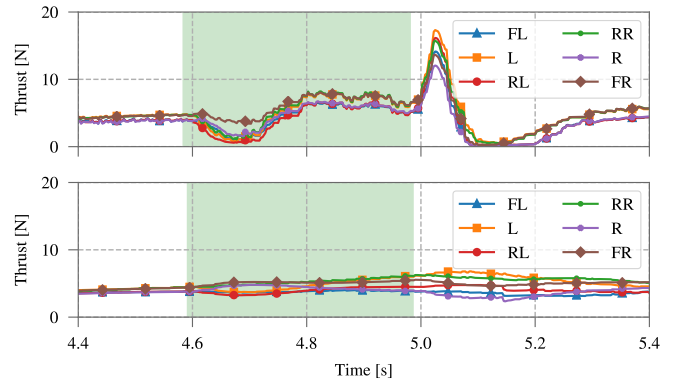


Fig. 15: Thrust control signals for the *4-Displacement* mission during the *well before task* disturbance. Top: R-MPC; Bottom: C-MPC. Shaded area indicates the disturbance is active. The motor reactions to the disturbance are almost imperceptible in C-MPC.

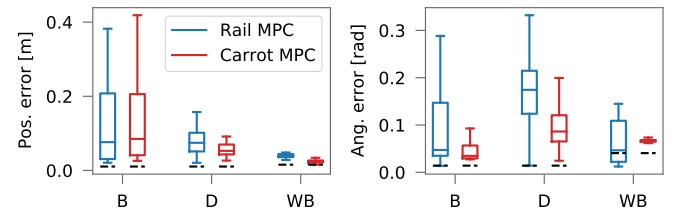


Fig. 16: Task error distributions for R-MPC and C-MPC. B: before task WP2. D: during WP2. WB: well before WP3. Dashed black lines indicate the error of the reference trajectory.

the mission itself. That is, C-MPC consumes much less energy than R-MPC to fulfill the same task.

For the sake of completeness and to confirm the behaviors anticipated in Fig. 14, we have performed a Monte Carlo simulation consisting of 50 experiments where a random disturbance is applied for each controller and each starting moment. The duration Δt and the magnitude F of the disturbance have been determined by randomly sampling the respective Gaussian distributions, $\Delta t [s] \sim \mathcal{N}(0.5, 0.25^2)$ and $F [N] \sim \mathcal{N}(8, 2^2)$. The starting time t_0 has been sampled from uniform distributions with ranges $[3.0, 3.2]$, $[3.7, 3.9]$ and $[4.4, 4.6]$ for the 'before', 'during' and 'well before' cases, respectively. The force is applied along the $[1, 1, 0]$ direction in the inertial coordinates. We show in Fig. 16 the resulting distributions of the norm of the position and orientation errors of the concerned tasks. We can see that C-MPC is generally more accurate (less error) and more predictable (less variance) than R-MPC. Notice that the orientation errors are larger in R-MPC than in C-MPC; this is due to UAW in R-MPC, which weights orientations less than position. Notice also the very predictable orientation error of C-MPC in the WB case: while this error is in great part due to an error of the reference trajectory, this indicates that the disturbances far enough from tasks do not alter the optimal way to fulfill the task.

Finally, it is worth mentioning that none of the nMPC controllers described in this work is capable of rejecting persistent disturbances (notice that all simulated disturbances are of temporal action). This is because the disturbances are not part of the model and the controller cannot account for

TABLE IV: Solver performance. N: nominal, D: with disturbance

	SOLVING TIME [ms]			# ITERATIONS		
	Mean	St. dev	Max.	Mean	St. dev	Max.
RAIL MPC						
<i>4-Displacement</i> (N)	2.58	1.02	18.4	1.52	0.51	4
<i>4-Displacement</i> (D)	2.92	1.13	15.4	1.49	0.51	4
<i>Eagle's Catch</i> (N)	2.02	0.78	10.5	1.24	0.43	3
CARROT MPC						
<i>4-Displacement</i> (N)	2.40	1.02	19.3	1.23	0.44	4
<i>4-Displacement</i> (D)	2.77	1.09	15.5	1.23	0.44	4
<i>Eagle's Catch</i> (N)	2.28	1.02	17.8	1.20	0.45	4

the discrepancy between the model and the reality if they are persistent. We believe that an external force observer would certainly improve this, however we consider it out of scope by now and leave its implementation as future work.

3) *Solver performance*: Any nMPC controller relies on an OCP solver that must be able to do one or more iterations in a very short time. In Table IV, we show some statistics related to the solving time per nMPC step, both in the *4-Displacement* and the *Eagle's Catch* missions. Notice that all the maximum values fit in the nMPC step of $\Delta t = 30\text{ms}$, thus enabling true nMPC control. However, highly dynamic platforms can run more smoothly and stably if the solver outputs a solution at higher rates, *e.g.* every time it receives an estimation of the state and before receiving the next one. In our 400Hz system this means solving in less than 2.5ms. As shown in Table IV, this is not always possible, as some of the means and all the maxima are above 2.5ms. In all the experiments of this paper the nMPC applies the control once the OCP has finished iterating and waits for the next state estimate to solve the next nMPC step. This suboptimal strategy has been proven sufficiently stable and accurate. We have described in Section VI-A a few possible improvements. Please refer to the conclusions below for further discussion.

VIII. CONCLUSIONS

We have proposed a full methodology to control UAMs based on full-body, torque-level, model predictive control. This methodology has been imported from the humanoid and legged robots community and adapted to the UAM. Such adaptation comprises some original contributions, particularly, in the methods to close the control loop through nMPC, which seem to be the most poorly explored by the original communities. We have explained the different parts in a way that can be regarded as a tutorial, for it is complete but avoids deviating too much from the main line of work constituting the current state of the art. These deviations range from techniques to add hard constraints to the solver, considering impacts in the treatment of contacts, the joint optimization of the timings in the mission plans, the online identification of the model and/or any persistent disturbance, or others. Some of these techniques can be explored in the provided references, while others might require new research.

The methods presented here have already proved their pertinence in the fields of humanoid and legged robotics with great success. In the area of UAM, in this paper we

have boarded the mathematical and software aspects, and have provided evidence of their maturity and fitness using realistic simulations that cover a wide range of platforms and challenging missions.

These techniques have yet to be demonstrated in real UAMs, and a few comments regarding our confidence in this proposal are necessary. First, we tested the algorithms in their basic versions and succeeded in generating accurate and stable motor commands for all experiments. We presented in Section VI-A possible improvements that should allow us to go beyond the performances displayed here. Second, we have run the algorithms single threaded in a standard CPU. Today, low weight CPUs suited for UAM such as the Intel[®] NUC 11¹² are already more powerful than our test bench CPU, and the FDDP algorithm accepts multithreading. These two aspects make us confident in the fact that processing power should not be an issue when moving to real UAMs, and we believe we can extend the prediction horizon beyond one second. Third and of special importance is tackling the electromechanics of the real implementation. This actually constitutes our immediate future work. Regarding the flying platform, accessing the motor drivers to send propeller speed commands can be done through open-source platforms such as the Pixhawk-4¹³ controller and PIX4¹⁴ libraries. The manipulator arms require significantly more attention, especially regarding light and high-torque motors, miniature power electronics and light arm structures. Fortunately, this way has been paved already by the legged robots community, for example through activities such as the Open Dynamic Robot Initiative¹⁵ [52] which proposes open-source torque-controlled 3D-printed links with torques up to 2.7Nm and weights below the 150g, based on which different arm configurations can be built. An important conclusion of the present study is that these arm specifications are sufficient to accomplish all the missions that we have simulated, and therefore that we can make real torque-controlled UAMs work with hardware (CPUs, motors, electronics and structures) available today.

ACKNOWLEDGMENTS

The authors would like to thank Nicolas Mansard at LAAS-CNRS in Toulouse and Carlos Mastalli at the University of Edinburgh for their support to get us started in the field of optimal control. Also, thanks to Arash Kalantari (NASA-JPL), for the collaboration in the project *Deployable self-adhering anchoring platform and its deployment system for future Mars Helicopters*, exploiting some of the concepts presented in this paper. Also, special thanks to Ricard Bordalba (IRI, CSIC-UPC) for his valuable feedback.

REFERENCES

- [1] J. Carpentier and P. Wieber, "Recent Progress in Legged Robots Locomotion Control," *HAL - Current Robotics Reports*, 2021.
- [2] J. Betts, *Practical Methods for Optimal Control and Estimation Using Nonlinear Programming*, 2nd ed. Cambridge University Press, 2009.

¹²<https://www.intel.com/content/www/us/en/products/details/nuc.html>

¹³https://docs.px4.io/master/en/flight_controller/pixhawk4.html

¹⁴<https://px4.io/>

¹⁵<https://open-dynamic-robot-initiative.github.io/>

- [3] F. Ruggiero, V. Lippiello, and A. Ollero, "Aerial manipulation: A literature review," *IEEE Robot. Automat. Lett.*, 2018.
- [4] K. H. B., F. Janabi-Sharifi, and A. Abdessameud, "Aerial manipulation: A literature survey," *Robotics and Autonomous Systems*, 2018.
- [5] F. Ruggiero, M. A. Trujillo, R. Cano, H. Ascorbe, A. Viguria, C. Perez, V. Lippiello, A. Ollero, and B. Siciliano, "A multilayer control for multirotor UAVs equipped with a servo," in *IEEE Int. Conf. Rob. Autom. (ICRA)*, 2015.
- [6] R. Rossi, A. Santamaria-Navarro, J. Andrade-Cetto, and P. Rocco, "Trajectory Generation for Unmanned Aerial Manipulators Through Quadratic Programming," *IEEE Robot. Automat. Lett.*, 2017.
- [7] V. Lippiello, J. Cacace, A. Santamaria-Navarro, J. Andrade-Cetto, M. A. Trujillo, Y. R. Rodríguez Esteves, and A. Viguria, "Hybrid Visual Servoing With Hierarchical Task Composition for Aerial Manipulation," *IEEE Robot. Automat. Lett.*, 2016.
- [8] S. Rajappa, M. Ryll, H. H. Bühlhoff, and A. Franchi, "Modeling, control and design optimization for a fully-actuated hexarotor aerial vehicle with tilted propellers," in *IEEE Int. Conf. Rob. Autom. (ICRA)*, 2015.
- [9] M. Tognon, E. Cataldi, H. A. T. Chavez, G. Antonelli, J. Cortés, and A. Franchi, "Control-aware Motion Planning for Task-Constrained Aerial Manipulation," *IEEE Robot. Automat. Lett.*, 2018.
- [10] M. J. Kim, K. Kondak, and C. Ott, "A Stabilizing Controller for Regulation of UAV With Manipulator," *IEEE Robot. Automat. Lett.*, 2018.
- [11] R. M. Murray, M. Rathinam, and W. Sluis, "Differential Flatness of Mechanical Control Systems: A Catalog of Prototype Systems," in *ASME Int. Congress and Exposition*, 1995.
- [12] M. Fliess, J. Levine, P. Martin, and P. Rouchon, "A Lie-Backlund approach to equivalence and flatness of nonlinear systems," *IEEE Tran. on Automatic Control*, 1999.
- [13] D. Mellinger and V. Kumar, "Minimum snap trajectory generation and control for quadrotors," in *IEEE Int. Conf. Rob. Autom. (ICRA)*, 2011.
- [14] K. Sreenath, N. Michael, and V. Kumar, "Trajectory generation and control of a quadrotor with a cable-suspended load - A differentially-flat hybrid system," in *IEEE Int. Conf. Rob. Autom. (ICRA)*, 2013.
- [15] B. Yüksel, G. Buondonno, and A. Franchi, "Differential flatness and control of protocentric aerial manipulators with any number of arms and mixed rigid-/elastic-joints," in *IEEE/RSJ Int. Conf. Intell. Rob. Sys. (IROS)*, 2016.
- [16] M. Tognon, B. Yüksel, G. Buondonno, and A. Franchi, "Dynamic decentralized control for protocentric aerial manipulators," in *IEEE Int. Conf. Rob. Autom. (ICRA)*, 2017.
- [17] M. Ryll, G. Muscio, F. Pierri, E. Cataldi, G. Antonelli, F. Caccavale, D. Bicego, and A. Franchi, "6D Interaction Control with Aerial Robots: The Flying End-Effector Paradigm," *Int. J. of Rob. Research*, 2019.
- [18] S. Hamaza, I. Georgilas, and T. Richardson, "An Adaptive-Compliance Manipulator for Contact-Based Aerial Applications," in *IEEE/ASME Int. Conf. Adv. Intell. Mechatronics (AIM)*, 2018.
- [19] M. Tognon, H. A. T. Chávez, E. Gasparin, Q. Sablé, D. Bicego, A. Mallet, M. Lany, G. Santi, B. Revaz, J. Cortés, and A. Franchi, "A Truly-Redundant Aerial Manipulator System With Application to Push-and-Slide Inspection in Industrial Plants," *IEEE Robot. Automat. Lett.*, 2019.
- [20] Q. Delamare, P. R. Giordano, and A. Franchi, "Toward aerial physical locomotion: The contact-fly-contact problem," *IEEE Robot. Automat. Lett.*, 2018.
- [21] D. Lunni, A. Santamaria-Navarro, R. Rossi, P. Rocco, L. Bascetta, and J. Andrade-Cetto, "Nonlinear model predictive control for aerial manipulation," in *IEEE Int. Conf. Unman. Aircr. (ICUAS)*, 2017.
- [22] G. Garimella and M. Kobilarov, "Towards model-predictive control for aerial pick-and-place," in *IEEE Int. Conf. Rob. Autom. (ICRA)*, 2015.
- [23] M. Geisert and N. Mansard, "Trajectory generation for quadrotor based systems using numerical optimal control," in *IEEE Int. Conf. Rob. Autom. (ICRA)*, 2016.
- [24] D. Tzoumanikas, F. Graule, Q. Yan, D. Shah, M. Popovic, and S. Leutenegger, "Aerial manipulation using hybrid force and position NMPC applied to aerial writing," in *Rob.: Sci. Sys. (RSS)*, 2020.
- [25] M. Kamel, K. Alexis, M. Achtelik, and R. Siegwart, "Fast nonlinear model predictive control for multicopter attitude tracking on so(3)," in *IEEE Conf. on Contr. Applications (CCA)*, 2015.
- [26] M. Neunert, C. d. Crousaz, F. Furrer, M. Kamel, F. Farshidian, R. Siegwart, and J. Buchli, "Fast nonlinear model predictive control for unified trajectory optimization and tracking," in *IEEE Int. Conf. Rob. Autom. (ICRA)*, 2016.
- [27] M. Brunner, K. Bodie, M. Kamel, M. Pantic, W. Zhang, J. Nieto, and R. Siegwart, "Trajectory tracking nonlinear model predictive control for an overactuated mav," in *IEEE Int. Conf. Rob. Autom. (ICRA)*, 2020.
- [28] D. Brescianini and R. D'Andrea, "Design, modeling and control of an omni-directional aerial vehicle," in *IEEE Int. Conf. Rob. Autom. (ICRA)*, 2016.
- [29] J. Nocedal and S. J. Wright, *Numerical Optimization*, 2nd ed. Springer, 2006.
- [30] A. Wächter and L. T. Biegler, "On the implementation of an interior-point filter line-search algorithm for large-scale nonlinear programming," *Mathematical Programming*, 2006.
- [31] R. H. Byrd, J. Nocedal, and R. A. Waltz, "KNITRO: An integrated package for nonlinear optimization," in *Large Scale Nonlinear Optimization*, 35–59, 2006, 2006.
- [32] D. Mayne, "A Second-order Gradient Method for Determining Optimal Trajectories of Non-linear Discrete-time Systems," *Int. J. of Contr.*, 1966.
- [33] W. Li and E. Todorov, "Iterative Linear Quadratic Design For Nonlinear Biological Movement Systems," in *Int. Conf. on Inf. in Contr., Autom. and Rob. (ICINCO)*, 2004.
- [34] A. Sideris and J. E. Bobrow, "An efficient sequential linear quadratic algorithm for solving nonlinear optimal control problems," in *IEEE American Control Conf.*, 2005.
- [35] M. Neunert, M. Stäuble, M. Gifftthaler, C. D. Bellicoso, J. Carius, C. Gehring, M. Hutter, and J. Buchli, "Whole-Body Nonlinear Model Predictive Control Through Contacts for Quadrupeds," *IEEE Robot. Automat. Lett.*, 2018.
- [36] J. Koenemann, A. Del Prete, Y. Tassa, T. E., O. Stasse, M. Bennewitz, and N. Mansard, "Whole-body model-predictive control applied to the HRP-2 humanoid," in *IEEE/RSJ Int. Conf. Intell. Rob. Sys. (IROS)*, 2015.
- [37] M. Gifftthaler, M. Neunert, M. Stäuble, J. Buchli, and M. Diehl, "A Family of Iterative Gauss-Newton Shooting Methods for Nonlinear Optimal Control," in *IEEE/RSJ Int. Conf. Intell. Rob. Sys. (IROS)*, 2018.
- [38] C. Mastalli, R. Budhiraja, W. Merkt, G. Saurel, B. Hammoud, M. Naveau, J. Carpentier, L. Righetti, S. Vijayakumar, and N. Mansard, "Crocodyl: An Efficient and Versatile Framework for Multi-Contact Optimal Control," in *IEEE Int. Conf. Rob. Autom. (ICRA)*, 2020.
- [39] T. A. Howell, B. E. Jackson, and Z. Manchester, "ALTRO: A Fast Solver for Constrained Trajectory Optimization," in *IEEE/RSJ Int. Conf. Intell. Rob. Sys. (IROS)*, 2019.
- [40] C. Mastalli, W. Merkt, J. Marti-Saumell, J. Solà, N. Mansard, and S. Vijayakumar, "A Direct-Indirect Hybridization Approach to Control-Limited DDP," *CoRR*, 2020.
- [41] S. E. Kazdadi, J. Carpentier, and J. Ponce, "Equality Constrained Differential Dynamic Programming," in *IEEE Int. Conf. Rob. Autom. (ICRA)*, 2021.
- [42] J. Martí-Saumell, J. Solà, C. Mastalli, and A. Santamaria-Navarro, "Squash-Box Feasibility Driven Differential Dynamic Programming," in *IEEE/RSJ Int. Conf. Intell. Rob. Sys. (IROS)*, 2020.
- [43] J. Solà, J. Deray, and D. Atchuthan, "A micro Lie theory for state estimation in robotics," *arXiv:1812.01537 [cs]*, 2018.
- [44] J. B. Rawlings, D. Q. Mayne, and M. Diehl, *Model predictive control: theory, computation, and design*. Nob Hill Publishing, 2017.
- [45] R. Featherstone, *Rigid body dynamics algorithms*. Springer, 2008.
- [46] R. Budhiraja, J. Carpentier, C. Mastalli, and N. Mansard, "Differential Dynamic Programming for Multi-Phase Rigid Contact Dynamics," in *IEEE Int. Conf. Hum. Rob. (ICHR)*, 2018.
- [47] M. Diehl, H. Bock, H. Diedam, and P.-B. Wieber, *Fast Motions in Biomechanics and Robotics: Optimization and Feedback Control*. Berlin, Heidelberg: Springer Berlin Heidelberg, 2006, ch. Fast Direct Multiple Shooting Algorithms for Optimal Robot Control, pp. 65–93.
- [48] S. Kleff, A. Meduri, R. Budhiraja, N. Mansard, and L. Righetti, "High-frequency nonlinear model predictive control of a manipulator," in *IEEE Int. Conf. Rob. Autom. (ICRA)*, 2021.
- [49] J. Carpentier, G. Saurel, G. Buondonno, J. Mirabel, F. Lamiroux, O. Stasse, and N. Mansard, "The Pinocchio C++ library : A fast and flexible implementation of rigid body dynamics algorithms and their analytical derivatives," in *IEEE Int. Sym. System Integration (SII)*, 2019.
- [50] F. Furrer, M. Burri, M. Achtelik, and R. Siegwart, *Robot Operating System (ROS): The Complete Reference (Volume 1)*. Cham: Springer International Publishing, 2016, ch. RotorS—A Modular Gazebo MAV Simulator Framework, pp. 595–625.
- [51] W. Blajer, "Methods for constraint violation suppression in the numerical simulation of constrained multibody systems – A comparative study," *Computer Methods in Applied Mechanics and Engineering*, 2011.
- [52] F. Grimminger, A. Meduri, M. Khadiv, J. Viereck, M. Wüthrich, M. Naveau, V. Berenz, S. Heim, F. Widmaier, T. Flayols, J. Fiene, A. Badri-Spröwitz, and L. Righetti, "An open torque-controlled modular robot architecture for legged locomotion research," *IEEE Robotics and Automation Letters*, vol. 5, no. 2, pp. 3650–3657, 2020.